

## RESEARCH ARTICLE

10.1002/2015JB012083

## Key Points:

- Gas hydrates on the Svalbard margin are most abundant north of the Knipovich Ridge
- Modeling shows that thermogenic methane contributes to the hydrate reservoir
- Up to 0.2 Mt hydrocarbons may have been produced off Svalbard since the Eocene

## Supporting Information:

- Text S1, Figures S1 and S2, and Table S1
- Table S2

## Correspondence to:

I. Dumke,  
ines.dumke@ntnu.no

## Citation:

Dumke, I., E. B. Burwicz, C. Berndt, D. Klaeschen, T. Feseker, W. H. Geissler, and S. Sarkar (2016), Gas hydrate distribution and hydrocarbon maturation north of the Knipovich Ridge, western Svalbard margin, *J. Geophys. Res. Solid Earth*, 121, 1405–1424, doi:10.1002/2015JB012083.

Received 15 APR 2015

Accepted 31 DEC 2015

Accepted article online 5 JAN 2016

Published online 30 MAR 2016

## Gas hydrate distribution and hydrocarbon maturation north of the Knipovich Ridge, western Svalbard margin

Ines Dumke<sup>1,2</sup>, Ewa B. Burwicz<sup>1</sup>, Christian Berndt<sup>1</sup>, Dirk Klaeschen<sup>1</sup>, Tomas Feseker<sup>3,4</sup>, Wolfram H. Geissler<sup>5</sup>, and Sudipta Sarkar<sup>1</sup>

<sup>1</sup>GEOMAR Helmholtz Centre for Ocean Research Kiel, Kiel, Germany, <sup>2</sup>Now at Department of Marine Technology, Norwegian University of Science and Technology, Trondheim, Norway, <sup>3</sup>MARUM - Center for Marine Environmental Sciences and Department of Geosciences, University of Bremen, Bremen, Germany, <sup>4</sup>Now at geoFact GmbH, Bonn, Germany, <sup>5</sup>Alfred Wegener Institute, Helmholtz Centre for Polar and Marine Research (AWI), Bremerhaven, Germany

**Abstract** A bottom-simulating reflector (BSR) occurs west of Svalbard in water depths exceeding 600 m, indicating that gas hydrate occurrence in marine sediments is more widespread in this region than anywhere else on the eastern North Atlantic margin. Regional BSR mapping shows the presence of hydrate and free gas in several areas, with the largest area located north of the Knipovich Ridge, a slow spreading ridge segment of the Mid Atlantic Ridge system. Here heat flow is high (up to 330 mW m<sup>-2</sup>), increasing toward the ridge axis. The coinciding maxima in across-margin BSR width and heat flow suggest that the Knipovich Ridge influenced methane generation in this area. This is supported by recent finds of thermogenic methane at cold seeps north of the ridge termination. To evaluate the source rock potential on the western Svalbard margin, we applied 1-D petroleum system modeling at three sites. The modeling shows that temperature and burial conditions near the ridge were sufficient to produce hydrocarbons. The bulk petroleum mass produced since the Eocene is at least 5 kt and could be as high as ~0.2 Mt. Most likely, source rocks are Miocene organic-rich sediments and a potential Eocene source rock that may exist in the area if early rifting created sufficiently deep depocenters. Thermogenic methane production could thus explain the more widespread presence of gas hydrates north of the Knipovich Ridge. The presence of microbial methane on the upper continental slope and shelf indicates that the origin of methane on the Svalbard margin varies spatially.

### 1. Introduction

Naturally occurring gas hydrates store large amounts of methane as well as other gaseous hydrocarbons and nonhydrocarbons. While microbial methane is typically considered as the dominant component of marine gas hydrates [Kvenvolden, 1995, and references therein], other sources of hydrocarbon such as thermogenic methane are often ignored. However, thermogenic methane may constitute a substantial component of hydrate-bound methane [e.g., Brooks et al., 1986; Ginsburg et al., 1992; Kvenvolden, 1995].

An appraisal of thermogenic methane stored in marine gas hydrates and later expelled at the seabed is crucial in several contexts. These include basin prospecting, evaluating source rock maturation, quantifying produced hydrocarbons, assessing hydrocarbon migration into and out of shallow hydrate reservoirs, and leakage into oceans and the atmosphere. Methane release from hydrates into the atmosphere has the potential to increase climate warming [e.g., Harvey and Huang, 1995]. This especially affects polar regions such as the northern North Atlantic, which are most sensitive to climate warming [Spielhagen et al., 2011] and host substantial gas hydrate reservoirs.

Most of the eastern North Atlantic margin lies within the zone of gas hydrate stability [Kretschmer et al., 2015]. However, gas hydrates have been detected in only three areas—on the Svalbard margin [Posewang and Mienert, 1999; Carcione et al., 2005; Vanneste et al., 2005a, 2005b; Bünz et al., 2008, 2012; Westbrook et al., 2009; Sarkar et al., 2012; Berndt et al., 2014b; Johnson et al., 2015; Plaza-Faverola et al., 2015], at the Storegga Slide headwall [Mienert et al., 1998; Bouriak et al., 2000; Bünz et al., 2003, 2005; Bünz and Mienert, 2004; Ivanov et al., 2007], and on the continental margin west of Ireland [Praeg et al., 2005]—even though free gas is also present in other parts of the margin, e.g., in the Vøring Basin [Kvenvolden et al., 1989; Svensen et al., 2004]. It is therefore important to study these areas in order to constrain the factors controlling the presence of gas hydrates.

On the western Svalbard margin, gas hydrates have been inferred at the continental slope where the base of the gas hydrate stability zone (BGHSZ) crops out at the seafloor in ~400 m water depth, causing active seepage [Westbrook *et al.*, 2009; Berndt *et al.*, 2014b]. Seepage is associated with hydrate dissociation that varies in extent and intensity depending on seasonal changes in bottom water temperatures [Berndt *et al.*, 2014b].

Farther west, gas hydrates are indicated by the presence of a bottom-simulating reflector (BSR) in seismic data [e.g., Vanneste *et al.*, 2005b; Sarkar *et al.*, 2012]. The BSR marks the interface between stable gas hydrates above and free gas below [Shipley *et al.*, 1979]. A large BSR area occurs north of the Knipovich Ridge [Vanneste *et al.*, 2005b], extending as far north as Vestnesa Ridge [Bünz *et al.*, 2008, 2012; Hustoft *et al.*, 2009]. Vanneste *et al.* [2005a] proposed that elevated heat flow of the Knipovich Ridge could promote the presence of gas and hydrates through increased thermogenic methane production.

Heat flow can be estimated from the depth of the BSR [Yamano *et al.*, 1982], which has been applied in a number of studies [e.g., Townend, 1997; Ganguly *et al.*, 2000; Kinoshita *et al.*, 2011] in order to assess the thermal situation of an area. This approach requires knowledge of the hydrate composition, bottom-water temperature, and thermal conductivity [Yamano *et al.*, 1982]. Similarly, if the temperature field is known it can be used to estimate the theoretical depth of the BSR [Hornbach *et al.*, 2012].

Using measured heat flow values, Vanneste *et al.* [2005b] found that the observed depth of the BSR agrees well with the theoretical BSR depth calculated for a pure-methane and seawater hydrate composition, from which they inferred a microbial origin of the gas. This is supported by the geochemical signatures of vent gas samples from the continental slope and outer shelf, which revealed gas compositions of >99.7% methane and average  $\delta^{13}\text{C}$  values of  $-55.7\text{‰}$  [Sahling *et al.*, 2014]. In contrast, a thermogenic origin is indicated by a  $\delta^{13}\text{C}$  of  $-45.7\text{‰}$  to  $-47.7\text{‰}$  (methane) and the presence of higher hydrocarbons ( $\text{C}_{3+}$ ) in hydrate samples collected at Vestnesa Ridge [Fisher *et al.*, 2011; Smith *et al.*, 2014]. Smith *et al.* [2014] attribute thermogenic methane production to the proximity of the Knipovich Ridge, which could promote maturation of organic matter.

Thermogenic methane production requires the presence of a source rock. An Eocene source rock exists in the Arctic Basin [Stein *et al.*, 2006; Mann *et al.*, 2009] and a Miocene source rock was drilled at Ocean Drilling Program (ODP) Site 909 north of the Hovgård Ridge [Shipboard Scientific Party, 1995b; Knies and Mann, 2002]. For the Arctic Basin, petroleum system modeling was used to determine maturity and petroleum generation potential of the Eocene source rock [Mann *et al.*, 2009]. For the Svalbard margin, the Miocene sequence is proposed to have a good to excellent source rock potential [Knies and Mann, 2002], but petroleum system modeling has not been applied.

Here we test the hypothesis that substantial amounts of methane stored in gas hydrate reservoirs on the western Svalbard margin result from thermogenic reactions within potential source rocks that are driven by higher heat flow in the vicinity of the slow spreading Knipovich Ridge. For this purpose, we (1) map the extent of gas hydrates on the Svalbard margin based on the BSR observed in seismic data, (2) assess the thermal situation north of the Knipovich Ridge using BSR-derived heat flow and probe measurements, and (3) evaluate the source rock potential via petroleum system modeling and determine if thermogenic methane can contribute to the gas hydrate reservoir.

## 2. Geological Setting

### 2.1. Tectonic Framework

The western Svalbard margin is tectonically a passive margin, but most of it lies within 100 km of the Mid-Atlantic Ridge system [Crane *et al.*, 1991]. Between 73°N and 82°N, the Mid-Atlantic Ridge system consists of four spreading segments—the Mohns Ridge, Knipovich Ridge, Molloy Ridge, and Lena Trough—that are offset by two transform faults (TF): the Molloy TF between the Knipovich and Molloy segments, and the Spitsbergen TF between the Molloy and Lena segments (Figure 1).

Before the opening of the North Atlantic, the Svalbard margin was characterized by the Spitsbergen Shear Zone, which comprised several elongate basins offset in an en-echelon manner [Crane *et al.*, 2001]. These basins were interpreted as pull-apart basins [Crane *et al.*, 1982, 1991; Thiede *et al.*, 1990]. Pull-apart rifting is often observed in major shear zones [e.g., Ebinger, 1989].

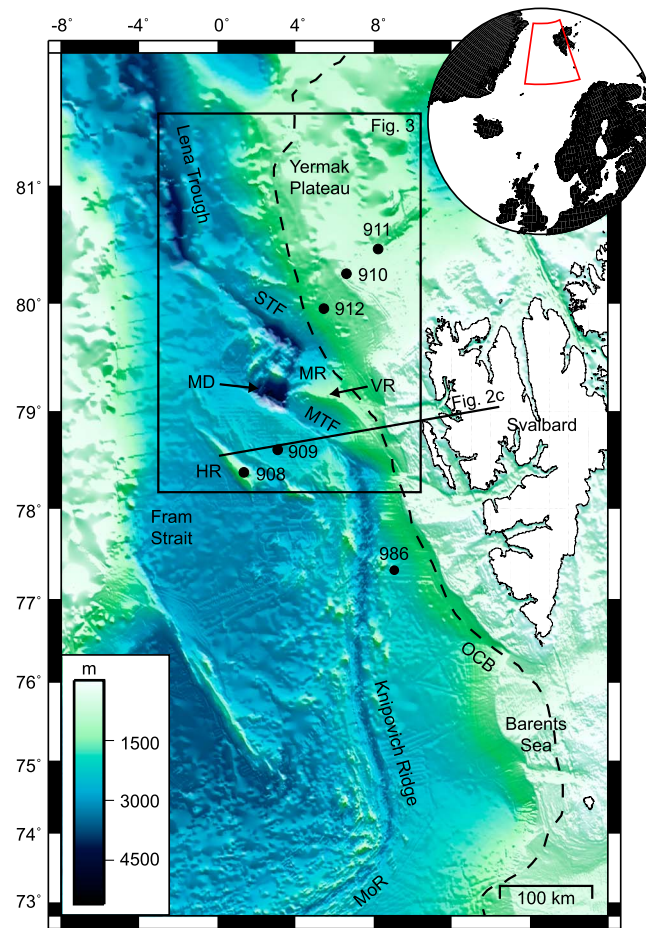


**Figure 1.** Bathymetric map of the western Svalbard margin, located in the northern North Atlantic (inset). Black dots mark locations of ODP boreholes. HR, Hovgård Ridge, MD, Molloy Deep, MTF, Molloy Transform Fault, MoR, Mohns Ridge, MR, Molloy Ridge, OCB, ocean-continent boundary after Engen *et al.* [2008], STF, Spitsbergen Transform Fault, VR, Vestnesa Ridge. Bathymetry is from the International Bathymetric Chart of the Arctic Ocean (IBCAO) grid [Jakobsson *et al.*, 2012].

The opening of the North Atlantic started in the early Eocene (~56 Ma) and proceeded from south to north [Talwani and Eldholm, 1977]. Seafloor spreading first occurred along the Mohns Ridge [Talwani and Eldholm, 1977], until the ridge encountered the ancient Spitsbergen Shear Zone. The spreading direction then changed abruptly as the Knipovich Ridge propagated into the N-S oriented shear zone [Crane *et al.*, 1988].

The timing for breakup along the Knipovich Ridge is unclear. While Eldholm *et al.* [1984] propose that seafloor spreading along the entire ridge was not established until middle Miocene, Crane *et al.* [1988, 1991] suggest that spreading accompanied by oceanic crust formation had reached the northern end of the ridge (around 78°N) by 40–50 Ma, only 5–10 Myr after the Mohns Ridge. However, Engen *et al.* [2008] inferred from magnetic anomalies that the present-day, regular mode of seafloor spreading did not establish until late Miocene (chron 5, 9.8 Ma).

Due to the abrupt change in direction, spreading along the Knipovich Ridge is asymmetric, with spreading rates being 1.5 times faster west of the ridge axis than east of it [Crane *et al.*, 1988]. Also, spreading rates decrease toward the north, from 4.3–4.9 mm yr<sup>-1</sup> at 75°N to generally <3 mm yr<sup>-1</sup> at 78°N [Crane *et al.*, 1988].

As spreading is slow compared to most other mid-ocean ridge segments, the Knipovich Ridge is classified as a slow to ultraslow spreading ridge [Dick *et al.*, 2003]. Slow spreading ridges commonly exhibit a central rift valley. At the Knipovich Ridge, the rift valley is 8–10 km wide and 3300–3700 m deep, and characterized by steep rift flanks [Crane *et al.*, 2001; Kvarven *et al.*, 2014].

## 2.2. Regional Stratigraphy and Hydrocarbon Source Rock Potential

Sediment thicknesses are 1–3 km along the western Svalbard margin, with the exception of Vestnesa Ridge, where thicknesses reach up to 5 km [Eiken and Hinz, 1993; Ritzmann *et al.*, 2004]. On the Knipovich Ridge, sediment thicknesses are ~1500 m on the eastern flank and 800–1000 m on the western flank [Kvarven *et al.*, 2014]. The difference is due to sediments from the Svalbard margin being mainly deposited against the eastern ridge flank [Crane *et al.*, 1988], whereas the western flank was cut off from sediment transport routes early in its development [Kvarven *et al.*, 2014].

Sedimentation rates on the margin are very high. Until middle Miocene, the sedimentation rate was ~100 mm yr<sup>-1</sup>; since then, it has increased to >300 mm yr<sup>-1</sup> [Myhre and Eldholm, 1988]. Due to several ice sheet advances across the shelf since 1 Ma [Faleide *et al.*, 1996], the areas near the shelf are characterized by glacial sediments [Eiken and Hinz, 1993]. In contrast, contourites dominate toward the ridges. The oldest

contourites are probably late Miocene to Pliocene in age [Eiken and Hinz, 1993], which is consistent with the establishment of an oceanic gateway between the Fram Strait and the Arctic Basin [e.g., Engen et al., 2008].

Several ODP drill holes provide information on the lithology of the marine sediments (Figure 1). However, at most sites drilling did not penetrate deeper than Pliocene sediments. The only exception is Site 909 north of the Hovgård Ridge, which was drilled down to Oligocene sediments [Myhre et al., 1995; Shipboard Scientific Party, 1995b]. The sediment recovered at Site 909 was mostly clay and silt. Four units (I, II, IIIA, and IIIB) can be distinguished based on varying amounts of organic material, dropstones, nannofossils, and carbonate (Table 1) [Shipboard Scientific Party, 1995b]. Unit IIIB (lower Miocene) is further divided into three subunits based on organic matter characteristics, i.e., total organic carbon (TOC), hydrogen index (HI), and vitrinite reflectance (Table 1) [Knies and Mann, 2002].

Unit IIIB has been interpreted as a potential source rock for hydrocarbon generation [Knies and Mann, 2002]. During the drilling process, the presence of methane as well as heavier hydrocarbons, which increased abruptly in concentration, required the termination of drilling at 1061.8 m below seafloor (mbsf) [Shipboard Scientific Party, 1995b]. Although Knies and Mann [2002] interpreted subunits 2 and 3 as presently immature based on vitrinite reflectance (0.4–0.5%), they suggested a fair to good source rock potential for unit IIIB. Source rock quality is proposed to increase (good to very good) toward the Hovgård Ridge and Svalbard margin, where the sequences are buried more deeply [Knies and Mann, 2002].

Another potential source rock is located further north in the Arctic Basin [Stein et al., 2006; Mann et al., 2009]. This source rock is of early to middle Eocene age and associated with the deposition of the freshwater fern *Azolla* [Mann et al., 2009]. On the Lomonosov Ridge, Integrated Ocean Drilling Program (IODP) boreholes [Expedition 302 Scientists, 2006] revealed a 93 m thick Eocene sequence of good to very good source rock potential [Stein, 2007]. Because of shallow (<200 m) burial of this sequence, in situ hydrocarbon generation was excluded for the Lomonosov Ridge; however, it may have occurred in the adjacent Amundsen Basin where the overburden is higher (>1000 m) [Mann et al., 2009].

### 2.3. Gas Hydrates on the Western Svalbard Margin

Gas hydrates on the Svalbard margin have been examined in detail over the last decade. Studies focused on the area north of the interception of the Knipovich Ridge and the Molloy TF [Posewang and Mienert, 1999; Carcione et al., 2005; Vanneste et al., 2005a, 2005b; Westbrook et al., 2008], as well as on Vestnesa Ridge [e.g., Vogt et al., 1999; Bünz et al., 2008, 2012; Hustoft et al., 2009; Plaza-Faverola et al., 2015] and offshore Prins Karls Forland where the predicted BGHSZ crops out at the seafloor [e.g., Westbrook et al., 2009; Berndt et al., 2014b].

The thickness of the gas hydrate stability zone (GHSZ) varies on the Svalbard margin. While the GHSZ tapers out at ~400 m water depth, resulting in zero thickness [Westbrook et al., 2009], it reaches thicknesses of up to 300 m toward the Lena Trough [Geissler et al., 2014b]. For a constant gas composition, thickness of the GHSZ, and hence the BSR depth, mainly depends on the geothermal gradient and the bottom water temperature, which decreases from >1.5°C on the upper slope to -0.9°C near the Molloy TF [Vanneste et al., 2005b].

Hydrate concentrations have been estimated in several studies, using seismic velocity data and theoretical models. The results generally range between 6% and 12% of the pore space [Vanneste et al., 2005a; Westbrook et al., 2008]. Carcione et al. [2005] calculated hydrate concentrations of up to 25%, but with an average of 7.2%. Hydrate concentrations also vary with depth, with the highest concentrations occurring near the BSR [Carcione et al., 2005].

Geochemical analyses were performed on hydrate samples recovered in two sediment cores on Vestnesa Ridge [Fisher et al., 2011; Smith et al., 2014], and another core from a seep site between Vestnesa Ridge and the continental slope [Fisher et al., 2011]. Also, gas bubbles emitted at the upper continental slope were sampled and analyzed [Sahling et al., 2014]. The results differ between the deepwater Vestnesa samples (~1200 m water depth) and the other, shallower (240–890 m water depth) samples. On Vestnesa Ridge, Smith et al. [2014] measured average hydrate compositions of 96.31% methane (C<sub>1</sub>), 3.36% ethane (C<sub>2</sub>), 0.21% propane (C<sub>3</sub>), 0.11% isobutane (i-C<sub>4</sub>), and 0.01% n-butane (n-C<sub>4</sub>), as well as δ<sup>13</sup>C values of -47.7‰ for C<sub>1</sub>, which agree with the -45.7 ± 2.7‰ of Fisher et al. [2011]. In contrast, the shallower samples from the slope reveal a composition of >99.7% methane and a δ<sup>13</sup>C of -55.7‰ [Sahling et al., 2014]. A similar

**Table 1.** Geological Model for 1-D Petroleum System Modeling<sup>a</sup>

Layer	Unit	Lithology	Z range (mbsf)	Thickness (m)	Epoch	Age (Ma)	TOC (%)	HI (mg HC/g TOC)	Vitrinite reflectance (%)
9		Water		(1) 2518 <sup>b</sup> (2A) 1670 (2B) 1465 (3A) 1670 (3B) 1465					
8	1 <sup>b</sup>	Clay, silty clay <sup>b</sup>	(1) 0–249 <sup>b</sup> (2A) 0–983 (2B) 0–885 (3A) 0–1172 (3B) 0–1055	(1) 249 <sup>b</sup> (2A) 983 (2B) 885 (3A) 1172 (3B) 1055	Quart. - Pliocene <sup>b</sup>	0–3.6			
7	11 <sup>b</sup>	Silty clay, clayey silt <sup>b</sup>	(1) 249–518 <sup>b</sup> (2A) 983–2046 (2B) 885–1841 (3A) 1172–2439 (3B) 1055–2195	(1) 269 <sup>b</sup> (2A) 1063 (2B) 956 (3A) 1267 (3B) 1140	Pliocene - Miocene <sup>b</sup>	3.6–10.0			
6	11a <sup>b</sup>	Silty clay, clayey silt <sup>b</sup>	(1) 518–923 <sup>b</sup> (2A) 2046–3645 (2B) 1841–3281 (3A) 2439–4345 (3B) 2195–3911	(1) 405 <sup>b</sup> (2A) 1599 (2B) 1440 (3A) 1906 (3B) 1716	Miocene <sup>b</sup>	10.0–13.5			
5	111b-1 <sup>c</sup>	Silty clay, clayey silt <sup>b</sup>	(1) 923–975 <sup>b,c</sup> (2A) 3645–3851 (2B) 3281–3466 (3A) 4345–4590 (3B) 3911–4131	(1) 52 <sup>b,c</sup> (2A) 206 (2B) 185 (3A) 245 (3B) 220	Miocene <sup>b</sup>	13.5–14.8 <sup>c</sup>	1.0 (0.8–1.2 <sup>b,c</sup> )	80 (30–130 <sup>b,e</sup> )	>1.0 <sup>c</sup>
4	111b-2 <sup>c</sup>	Silty clay, clayey silt <sup>b</sup>	(1) 975–1023 <sup>b,c</sup> (2A) 3851–4040 (2B) 3466–3636 (3A) 4590–4816 (3B) 4131–4335	(1) 48 <sup>b,c</sup> (2A) 189 (2B) 170 (3A) 226 (3B) 204	Miocene <sup>b</sup>	14.8–16.2 <sup>c</sup>	1.0 (0.8–1.2 <sup>b,c</sup> )	80 (30–130 <sup>b,e</sup> )	>1.0 <sup>c</sup>
3	111b-3 <sup>c</sup> / 1/6 <sup>d</sup>	Silty clay, clayey silt <sup>b,d</sup>	(1) 1023–1062 <sup>b,c,d</sup> (2A) 4040–4194 (2B) 3636–3775 (3A) 4816–5000 (3B) 4335–4500	(1) 39 <sup>b,c,d</sup> (2A) 154 (2B) 139 (3A) 184 (3B) 165	Mid-Miocene <sup>b,c</sup> - Mid-Eocene <sup>c</sup>	16.2 <sup>c</sup> –44.0	2.5 (2.0–3.0 <sup>b,c</sup> )	170 (140–250 <sup>b,e</sup> )	0.4–0.5 <sup>c</sup>
2	2 <sup>d</sup>	Biosiliceous ooze <sup>d</sup>	(1) 1062–1155 <sup>d</sup> (2A) 4194–4562 (2B) 3775–4105 (3A) – (3B) –	(1) 93 <sup>d</sup> (2A) 368 (2B) 330 (3A) – (3B) –	Mid-Eocene <sup>d</sup>	44.0 <sup>d</sup> –50.0	2.5 (2.0–3.0 <sup>d</sup> )	200 (150–350 <sup>d,f</sup> )	0.25 <sup>f</sup>
1	3 <sup>d</sup>	Clay, silty clay <sup>d</sup>	(1) 1155–1266 <sup>d</sup> (2A) 4562–5000 (2B) 4105–4500 (3A) – (3B) –	(1) 111 <sup>d</sup> (2A) 438 (2B) 395 (3A) – (3B) –	Late Paleocene - Mid-Eocene <sup>d</sup>	50.0–56.0 <sup>f</sup>	1.8 (1.0–2.5 <sup>d</sup> )	150 (50–300 <sup>d,f</sup> )	<0.5 <sup>f</sup>

<sup>a</sup>Depth ranges and layer thicknesses differ for the model runs: (1) ODP site 909 as reference: normal stratigraphy (only Miocene source rock) and with Eocene added underneath; (2A) Miocene + Eocene source rock for site A (scaled to 5 km sediment thickness); (2B) Miocene + Eocene source rock for site B (scaled to 4.5 km); (3A) Miocene source rock for site A (scaled to 5 km); (3B) Miocene source rock for site B (scaled to 4.5 km). TOC and HI are given as "mean (min-max)".

<sup>b</sup>Shipboard Scientific Party [1995b].

<sup>c</sup>Knies and Mann [2002].

<sup>d</sup>Expedition 302 Scientists [2006].

<sup>e</sup>Stein and Strax [1996].

<sup>f</sup>Stein et al. [2006].

$\delta^{13}\text{C}$  value of  $-54.6 \pm 1.7\text{‰}$  was measured at the plume field site [Fisher *et al.*, 2011]. On the shelf, isotopic signatures indicated a mainly microbial origin; however, Knies *et al.* [2004] also found evidence for migrated thermogenic gas, e.g., in the Van Mijenfjorden and Storfjorden.

The isotopic signatures suggest that the origin of the observed gas is spatially variant. While the results of Knies *et al.* [2004], Fisher *et al.* [2011], and Sahling *et al.* [2014] support a microbial origin for the shelf and water depth down to about 800 m; Smith *et al.* [2014] suggest at least partially thermogenic methane production, which is inferred from the heavier  $\delta^{13}\text{C}$  values and the presence of higher hydrocarbons ( $\text{C}_{3+}$ ). Thermogenic gas production also occurs close to the coast of the Kongsfjord [Knies *et al.*, 2004]. Alternatively, it has been discussed that some of the gas could be sourced from serpentinization of the oceanic basement [Rajan *et al.*, 2012; Johnson *et al.*, 2015]. However, Smith *et al.* [2014] argue that the involvement of serpentinization would require heavier  $\delta^{13}\text{C}$  values of around  $-25\text{‰}$ , which are not observed.

### 3. Materials and Methods

#### 3.1. Reflection Seismic Data

During RV Maria S. Merian cruise MSM21/4 in 2012, we acquired multichannel 2-D seismic (MCS) data at the northern end of the Knipovich Ridge [Berndt *et al.*, 2014a]. The data were recorded using a 120-channel streamer and an 88-channel streamer. The data were sampled at 2 kHz, and the recording length was 5.0–6.5 s. A GI-Gun ( $2 \times 1.7$  l) was used as a source and operated at a shot interval of 6–8 s.

Positions for each channel were calculated by backtracking along the profiles from the GI-Gun GPS positions. The shot gathers were analyzed for abnormal amplitudes below the seafloor reflection by comparing neighboring traces in different frequency bands within sliding time windows. To suppress surface-generated water noise, a  $\tau$ -p filter was applied in the shot gather domain. Common midpoint (CMP) profiles were then generated through crooked-line binning with a CMP spacing of 1.5625 m. A zero-phase band-pass filter was applied to the data, using corner frequencies of 60 Hz and 360 Hz. Based on regional velocity information from MCS data [Sarkar *et al.*, 2015], an interpolated and extrapolated 3-D interval velocity model was created below the digitized seafloor reflection of the high-resolution streamer data. This velocity model was used to apply a CMP stack and an amplitude-preserving Kirchhoff post-stack time migration.

In addition, we used 2-D seismic data acquired along the Svalbard margin and in the Fram Strait during cruises JR211 in 2008 (see Sarkar *et al.* [2012] for more details) and MSM31 in 2013 [Geissler *et al.*, 2014a], as well as seismic data provided by AWI Bremerhaven [Geissler *et al.*, 2011, 2014b]. All data underwent standard processing including time migration.

#### 3.2. Heat Flow Measurements

In situ measurements of sediment temperature and thermal conductivity were performed during cruise MSM21/4, using a standard violin-bow-type heat flow probe by FIELAX GmbH, Bremerhaven. The probe consists of 22 temperature sensors distributed evenly over an active length of 5.46 m. The sensors were calibrated to a precision of  $0.002^\circ\text{C}$  at a water depth of 1400 m.

We conducted measurements at four stations. Each time, the sediment temperature profile was measured for 7 min after penetration into the sediment. Equilibrium temperatures were obtained by extrapolation from the recorded time series, using the method of Villinger and Davis [1987]. After the temperature measurement, thermal conductivity was determined by measuring the decay of a heat pulse emitted from a heater wire along the entire length of the probe.

#### 3.3. BSR-Based Heat Flow Calculation

##### 3.3.1. Calculation Method

Geothermal gradients and heat flow were calculated from the BSR observed in the seismic data of cruises MSM21/4 and JR211, using the method after Yamano *et al.* [1982]. This method requires knowledge of the depth of the BSR and seafloor, the phase relation of the hydrate system, and the thermal conductivity of the sediments.

The BSR and seafloor were picked in the seismic data using the Kingdom Suite software (IHS). The picks were then exported to Matlab® (Mathworks Inc.) and converted to depth. We applied a basic velocity model based

on MSM21/4 conductivity-temperature-depth (CTD) data and depth-migrated seismic data from cruise JR211, with velocities of  $1460 \text{ m s}^{-1}$  for the water layer and  $1695 \text{ m s}^{-1}$  between seafloor and BSR.

To determine the pressure at BSR level, we assumed hydrostatic pressure [Townend, 1997; Kinoshita *et al.*, 2011; Li *et al.*, 2012; Martin *et al.*, 2004]. We used a seawater density of  $1027 \text{ kg m}^{-3}$  [Ehlers and Jokat, 2013].

To calculate temperatures at the BSR, several studies [e.g., Li *et al.*, 2012; Martin *et al.*, 2004; Ganguly *et al.*, 2000] used the methane hydrate stability curve of Dickens and Quinby-Hunt [1994]. However, this curve is valid only for pressures of up to 10 MPa, whereas our data reached pressures of up to 35 MPa. We therefore applied the CSMHYD program by Sloan [1998] to generate a new curve of methane hydrate stability (Figure S1 in the supporting information), using as components seawater (pure water +3.5 wt % NaCl) and the hydrate composition of Smith *et al.* [2014] from Vestnesa Ridge. This approach resulted in the following equation

$$T_{\text{BSR}} = 7.5877 \ln(p_{\text{BSR}}) + 216.76 \quad (1)$$

where  $p_{\text{BSR}}$  (in kPa) is the pressure at BSR level. The resulting  $T_{\text{BSR}}$  is given in K.

The geothermal gradient was calculated via

$$\text{gradT} = \frac{dT}{dz} = \frac{T_{\text{BSR}} - T_{\text{sea}}}{z_{\text{BSR}}} \quad (2)$$

where gradT is in  $\text{K km}^{-1}$ ;  $T_{\text{BSR}}$  and  $T_{\text{sea}}$  (in K) are the temperatures at the BSR and the seafloor, respectively; and  $z_{\text{BSR}}$  is the depth of the BSR in mbsf. We assumed that seafloor temperatures are equal to bottom-water temperatures, which vary in the study area due to the large water depth range from <1000 m to >3000 m. We therefore used a seafloor temperature-depth function based on CTD data of MSM21/4 and Sarkar *et al.* [2015].

Heat flow was then calculated by

$$H = k \times \text{gradT} \quad (3)$$

where  $H$  is in  $\text{mW m}^{-2}$ ,  $k$  (in  $\text{W m}^{-1} \text{K}^{-1}$ ) is the thermal conductivity of the sediments, and gradT (in  $\text{K km}^{-1}$ ) is the geothermal gradient. For the thermal conductivity, a constant value of  $1.3 \text{ W m}^{-1} \text{K}^{-1}$  was chosen, which is the average of thermal conductivities measured at ODP sites 908 and 909 [Shipboard Scientific Party, 1995a, 1995b]. This calculation method was associated with final absolute uncertainties of 11–24% for the geothermal gradient and 19–34% for the heat flow (see supporting information).

### 3.4. 1-D Petroleum System Modeling

We used the PetroMod software by Schlumberger for the numerical modeling of potential hydrocarbon generation on the Svalbard margin. The modeling was conducted at two sites chosen based on their different heat flow characteristics and locations with respect to the Knipovich Ridge axis: site A was located north of the present ridge axis in 1670 m water depth, while site B (1465 m water depth) was east of the ridge and landward of the ocean-continent boundary of Engen *et al.* [2008] (Figure 2a). Site 909 (2518 m water depth) was used as a reference site.

The modeling method involved a full 1-D reconstruction of the basin stratigraphy at the modeling sites throughout their geological history. First, present-day geological layers were back-stripped to give a proxy for initial layer thicknesses, ages, and densities at the time of deposition. The decompacted sedimentary layers were then used to restore stratigraphic units separately for each site. Standard values for physical properties of dominant lithologies (mostly clays and silts; Table 1), including initial seafloor porosity, compaction length scale, density, and permeability as well as thermal properties (thermal conductivity, heat capacity, and radiogenic heat), were taken from the inbuilt PetroMod library. Finally, a multilayer package including assigned stratigraphy, lithology, ages of layers, and their potential hydrocarbon productivity was derived and used as a base for four modeling runs.

#### 3.4.1. Modeling Input

Due to a lack of precise paleo-bathymetry and paleo-temperature data, boundary conditions assuming constant water depths and a constant seafloor/bottom-water temperature of  $2^\circ\text{C}$  were assigned over the entire history of the modeled sites.

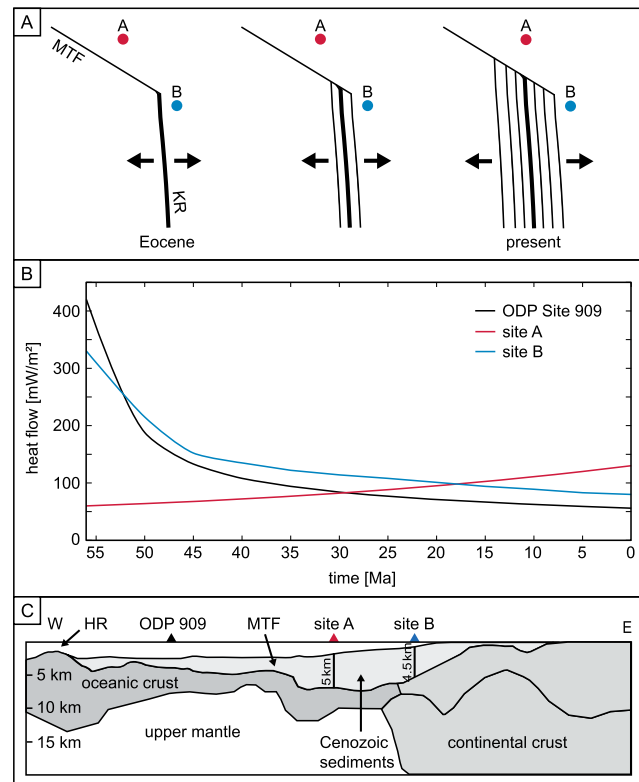


**Figure 2.** Heat flow evolution at the two modeling sites, following Eocene breakup along the Knipovich Ridge (KR). (a) As rifting progressed, the spreading axis moved away from site B and toward site A, causing heat flow to increase at site A and decrease at site B. MTF, Molloy Transform Fault. (b) Heat flow curves for site A, site B, and ODP Site 909. (c) Schematic of a crustal transect from Hovgård Ridge (HR) to Kongsfjorden, illustrating total sediment thicknesses at sites A and B. Note that sites A, B, and ODP 909 are not located on this transect but have been projected onto it. Transect location is shown in Figure 1. MTF, Molloy Transform Fault. After Ritzmann et al. [2004].

derived from the BSR (Figure 2b). The cooling curve of site B is exponential, with a decrease from 330 mW m<sup>-2</sup>, corresponding to the maximum heat flow observed today in the center of the rift, to the present heat flow of 80 mW m<sup>-2</sup> (Figure 2b). For Site 909, we derived a heat flow curve from the plate cooling curve of Sundvor et al. [2000] (Figure 2b).

**3.4.1.2. Geological Model**

There are no deep drill sites in the area north of the Knipovich Ridge, and hence, stratigraphic information is not available, which complicated the design of a geological input model. The closest ODP site is Site 909 (Figure 1), and we therefore assumed the same lithology at our modeling sites (Table 1), including the Miocene sequence that was interpreted as a potential but immature source rock (unit IIIb in Knies and Mann [2002]). The hydrocarbon generation potential of the source rock depends on its initial TOC content and HI, which we obtained from the literature as detailed in Table 1.

In addition to a Miocene source rock, we also tested the hydrocarbon generation potential for a potential Eocene source rock with the same characteristics as the Eocene sediments in the Arctic Basin [Mann et al. 2009]. The Eocene layers, corresponding to layers 1–3 of IODP sites M0002–M0004 in the Arctic Basin [Expedition 302 Scientists, 2006], were therefore added underneath the stratigraphic record from Site 909. As the lithology and Eocene-Miocene age of unit IIIb of Site 909 agreed well with unit 1/6 of sites M0002–M0004, they were treated as one layer in the geological model. The geological model for sites A and B thus consisted of nine layers including the water layer (layer 9), Miocene source rock (layers 3–5), and Eocene source rock (layers 1–2) (Table 1).

**3.4.1.1. Heat Flow**

An important input for the petroleum system modeling was the thermal history at the modeling sites. As the precise onset of seafloor spreading at the Knipovich Ridge and the timing of breakup differ [e.g., Eldholm et al., 1984; Crane et al., 1991; Engen et al., 2008], we assumed that heat flow changed at sites A and B as spreading along the ridge progressed. Over time, the spreading axis moved westward, away from site B and toward site A (Figure 2a). Site A thus experienced heating, while site B was characterized by cooling.

As we only knew the present-day heat flow inferred from the BSR, we made assumptions regarding the heat flow evolution since the initiation of rifting. For site A, we assumed a regional background heat flow for the Eocene. The present-day background heat flow on the Svalbard/Yermak margin is 75–100 mW m<sup>-2</sup>, but heat flow must have been lower before rifting introduced more heat to the margin. We therefore chose a heat flow of 60 mW m<sup>-2</sup>, similar to today's background heat flow on the Barents Sea/Norwegian margin (50–75 mW m<sup>-2</sup>) [Vogt and Sundvor, 1996]. The heat flow curve at site A then moderately increases from 60 mW m<sup>-2</sup> to 130 mW m<sup>-2</sup>

Cenozoic sediment thicknesses down to the basement were inferred from a wide-angle seismic transect of *Ritzmann et al.* [2004] from Kongsfjorden to Hovgård Ridge. Total sediment thicknesses amount to 5 km at site A and 4.5 km at site B (Figure 2c), which is supported by *Geissler et al.* [2011]. The layer thicknesses inferred from the ODP and IODP sites were scaled to these thicknesses as detailed in section 3.4.2.

#### 3.4.1.3. Kinetics

Kinetics of hydrocarbon generation is not known for the Svalbard margin or for the North Atlantic-Artic region, in general. We therefore used standard global kinetics from *Pepper and Corvi* [1995] (type B, siliclastic lithofacies in marine environments) for both source rocks. This general kinetics was previously tested in modeling of hydrocarbon generation from specific kerogen organofacies with separate oil and gas fractions. The type B kinetics implies an oil to gas ratio of 83% to 17% [*Pepper and Corvi*, 1995].

#### 3.4.2. Modeling Approach

We tested several 1-D modeling approaches of the hydrocarbon generation process without considering migration of oil and/or gas fractions. Determination of the regional impact of gas migration toward the GHSZ and subsequent potential hydrate formation or fluid venting is therefore beyond the scope of this study.

Hydrocarbon generation was modeled with a constant time step of 1 Ma and a vertical resolution of 10 m during four separate runs, which mainly differ in the layer thicknesses applied (Table 1). Run 1 (Site 909) was used as a reference and involved modeling for a Miocene source rock with and without an Eocene source rock. Run 2 included a Miocene and an Eocene source rock at sites A and B, with the stratigraphy scaled to total sediment thicknesses of 5 km and 4.5 km, respectively. Run 3 involved only the Miocene source rock (layers 3–9 in Table 1), again with total sediment thicknesses of 5 km and 4.5 km for sites A and B, respectively. Runs 2 and 3 were conducted three times for mean, minimum, and maximum TOC and HI values as shown in Table 1. The model runs with minimum and maximum TOC and HI represented lower and upper error bounds, respectively.

Run 4 served to model hydrocarbon generation from the Miocene source rock for a series of thinner overburdens at sites A and B to account for the possibility of total sediment thicknesses lower than those used in Runs 2 and 3. Starting with the original layer thicknesses of ODP site 909 (100%), layer thicknesses were increased at 50% intervals to 350% of the original thicknesses (Table S2 in the supporting information). Hydrocarbon generation was modeled for each case and compared to the results of Run 3. Run 4 involved mean TOC and HI values at both site A and site B, which differed in their water depths and thus in the thickness of layer 9.

## 4. Results

### 4.1. BSR Distribution

Based on the available seismic lines, we identified three main centers of BSR occurrence on the Svalbard margin (Figure 3). All three are located in the vicinity of spreading segments, i.e., the Knipovich Ridge, the Molloy Ridge, and the Lena Trough.

The southernmost and largest area of BSR occurrence lies close to the northern end of the Knipovich Ridge. It covers an area of  $\sim 3500$  km<sup>2</sup> and extends in a northwestern direction along the Molloy TF, with a width of up to 40 km. The BSR is mostly found in the area northeast of the Molloy TF, but also occurs in a few locations on the western flank of the Knipovich Ridge. As the southern BSR area also has the best data coverage, we will focus on this area for the rest of the paper and refer to it as our study area.

The other two BSR areas are located east of the Lena Trough (2400 km<sup>2</sup>) [*Geissler et al.*, 2014b] and north of the Molloy Ridge. The Molloy Ridge BSR area covers  $\sim 1400$  km<sup>2</sup> and extends to the northwest, parallel to the Spitsbergen TF. There is another, smaller ( $\sim 300$  km<sup>2</sup>) BSR area inferred from JR211 profiles located northeast of Vestnesa Ridge at the eastern end of the Spitsbergen TF.

In between the centers of BSR occurrence, we observed two types of BSR gaps: (1) apparent gaps, where seismic data are not available and hence it is not known whether a BSR does exist, and (2) true gaps for which seismic data exist but lack a BSR. True gaps were, for example, found west of Vestnesa Ridge and the Molloy TF [*Vanneste et al.*, 2005b]. For most parts of the Lena Trough and southern BSR areas, a BSR was also absent east of the ocean-continent boundary of *Engen et al.* [2008]. In addition, a BSR was not observed along some of the seismic lines of *Geissler et al.* [2014b], e.g., on the southernmost lines and south of the Lena Trough

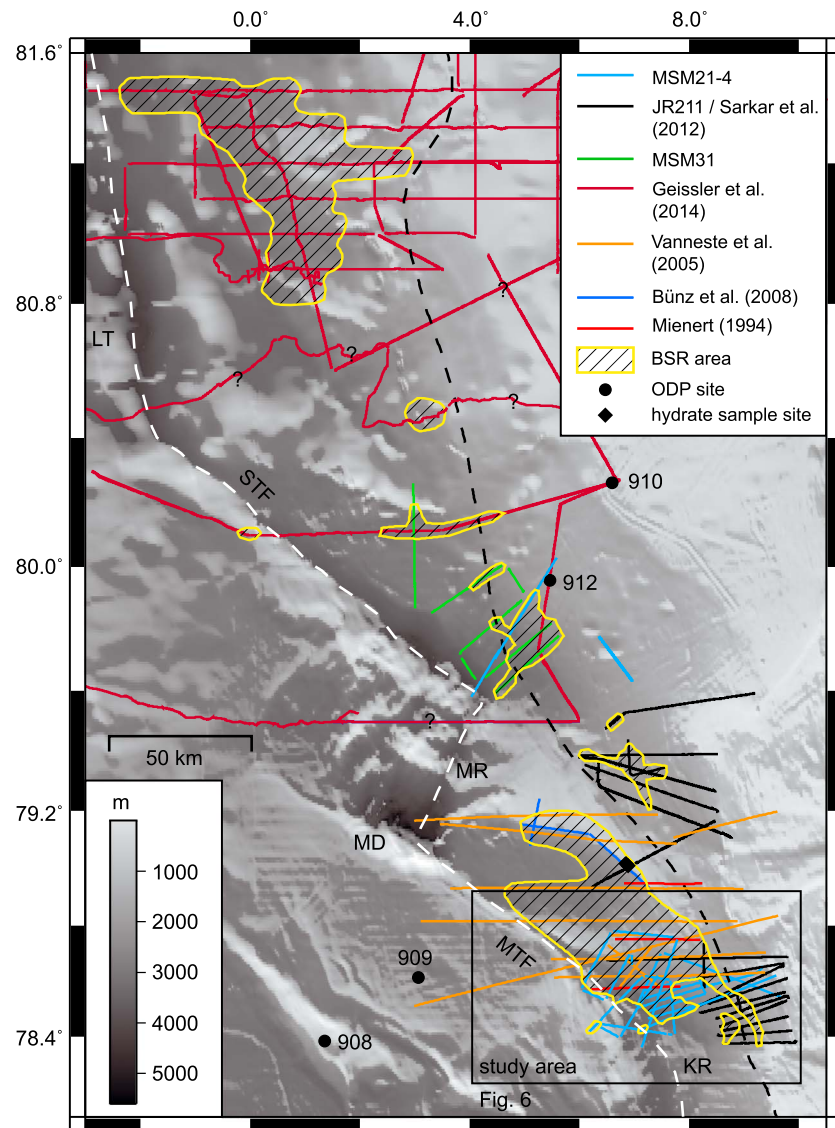


**Figure 3.** Map of the BSR distribution along the Svalbard margin, based on 2-D seismic data collected on different surveys. The BSR indicates the presence of gas hydrates. Stippled lines mark the ocean-continent boundary after Engen *et al.* [2008] (black) and the present-day plate boundary (white). Black dots mark ODP site locations. Question marks indicate profile sections where the seismic data are not conclusive about the existence of a BSR. Figure location is shown in Figure 1. LT, Lena Trough, MD, Molloy Deep, MTF, Molloy Transform Fault, MR, Molloy Ridge, SFZ, Spitsbergen Fracture Zone. Bathymetry is from the IBCAO grid [Jakobsson *et al.*, 2012].

BSR area, where a BSR was absent except for an ~13 km long-profile section. However, these data are of lower resolution, which made BSR identification difficult, and hence, the presence of hydrate cannot be excluded completely along these profiles.

In general, gas hydrate can also be present without a BSR [Haacke *et al.*, 2007], because a BSR depends on the lithology besides the existence of free gas. Alternatively, a BSR could be hidden in case of parallel sediment layering, which may apply to some of the profiles of Geissler *et al.* [2014b]. Consequently, the gas hydrate extent inferred from the presence of a BSR in seismic data is considered a minimum extent.

**4.2. BSR Character**

The BSR is well imaged in the MSM21/4 and JR211 seismic data sets (see also Sarkar *et al.* [2012] for a description of the JR211 data). It is characterized by a reflection of negative polarity that generally follows the

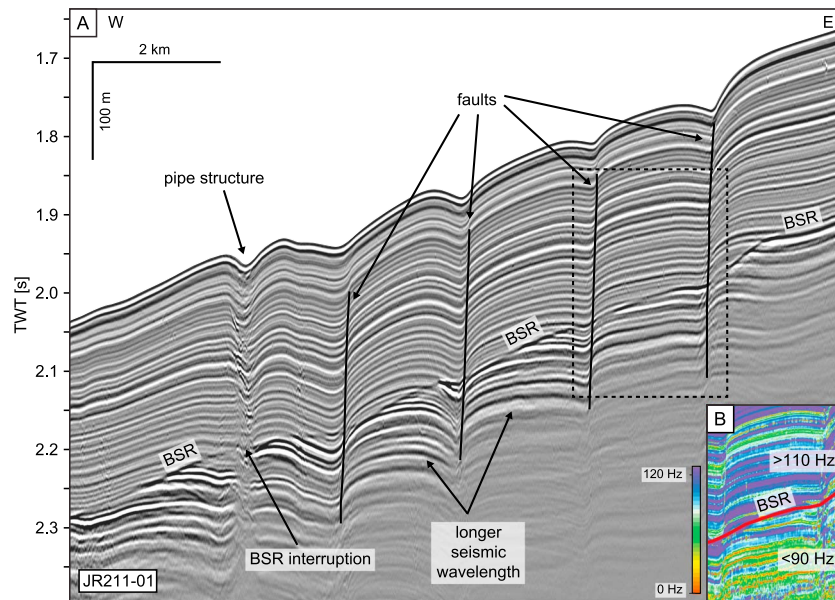


**Figure 4.** (a) Example of a well-imaged long BSR (>18 km, continuing outside the section shown here) along profile JR211-01. At the near-vertical faults, the BSR is undisturbed, but it is interrupted and slightly up-bending at the pipe structure, indicating a change in the thermal field. The pipe structure is characterized by downbending, slightly chaotic reflections. Stippled rectangle marks the inset shown in Figure 4b. (b) Instantaneous frequency attribute of the same section. The frequency of the reflected seismic signal differs strongly between the sediments above the BSR (>110 Hz) and below (<90 Hz), indicating strong attenuation of higher frequencies. Location is shown in Figure 6.

seafloor (Figures 4a and 5a) at a depth of 90–290 mbsf (on average 200 mbsf). Enhanced amplitudes are observed immediately beneath the BSR (Figure 5a). On most profiles, the BSR is either continuous over distances of 8–18 km (Figure 4a), or shorter and often interrupted (Figure 5a).

Some profiles show a distinct change from a normal seismic reflection character above the BSR to higher amplitudes and larger seismic wavelengths below the BSR (Figure 4a). This boundary is also very obvious in the instantaneous frequency attribute of the seismic data (Figure 4b), which indicate a drop from >110 Hz above the BSR to <90 Hz below, and thus a strong attenuation of higher seismic frequencies at the BSR. This anomaly occurs in a >360 km<sup>2</sup> large area about 20 km north of the Knipovich Ridge (Figure 6a) and is observed in both the MSM21/4 and JR211 data.

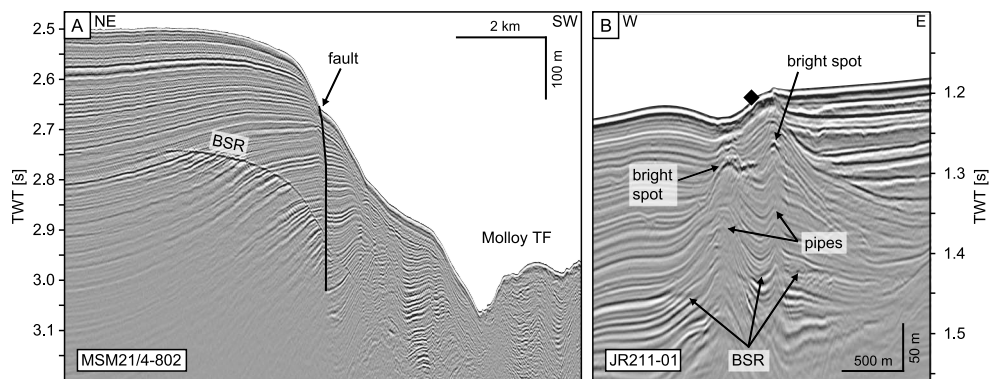


**Figure 5.** (a) Shorter, well-imaged BSR on the northeast of the Molloy Transform Fault. The BSR is not interrupted by the near-vertical normal fault. (b) Two pipes characterized by up-bending reflectors, bright spots, and an interrupted BSR. Black diamond shape marks the shallower sample site of Fisher *et al.* [2011]. Locations are shown in Figure 6.

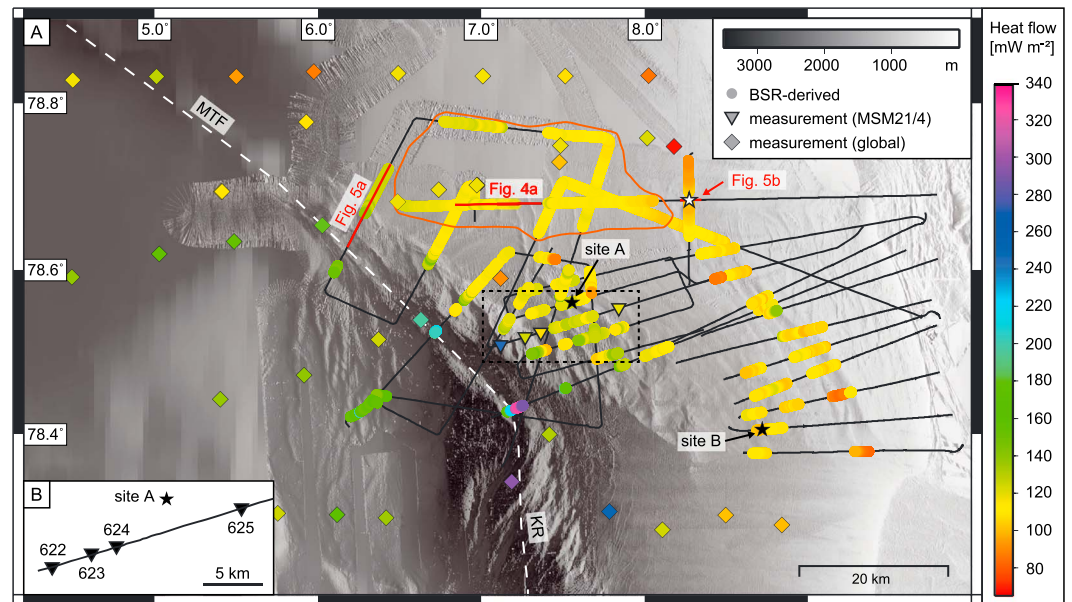


**Figure 6.** (a) Heat flow map showing the BSR-derived values along with heat flow measurements at the northern end of the Knipovich Ridge. Black stars mark sites A and B for which the petroleum system modeling was carried out in order to test the hydrocarbon generation potential of the area. The white star marks the shallower sample site of Fisher et al. [2011]. The red polygon indicates the area in which strong attenuation of seismic frequencies below the BSR was observed (shown in Figure 4a) White stippled line marks the present-day rift boundary. Stippled rectangle shows location of the inset shown in Figure 6b. Location is shown in Figure 3. KR, Knipovich Ridge, MTF, Molloy Transform Fault. Bathymetry is from the IBCAO grid [Jakobsson et al., 2012]. (b) Inset showing heat flow stations of cruise MSM21/4.

### 4.3. Vertical Seismic Anomalies

Two types of vertical seismic anomalies exist in the study area: faults and pipe structures (see also Sarkar et al. [2012]). The faults are mostly near-vertical normal faults, many of which do not reach the seafloor. Where a BSR is present at a fault, the BSR remains undisturbed (Figures 4a and 5a).

Five pipes were identified in the study area: three are characterized by up-bending and two by down-bending reflections. Up-bending pipes are narrow (100–150 m) and do not reach the seafloor, with two of them terminating at bright spots. The two down-bending pipes are ~230 m and ~340 m wide and show a chaotic internal reflection pattern (Figure 4a). They reach the seafloor where they terminate in ~5–10 m deep depressions. All pipe structures occur where a BSR is present, and at each pipe the BSR is interrupted and sometimes vertically offset on the other side of the pipe (Figure 4a).

In addition, there are two vertical anomalies characterized by reduced seismic amplitudes. One of these, an ~400 m wide structure located outside the BSR area, has been described as a chimney structure [Sarkar et al., 2012]. The other anomaly is >1.5 km wide and comprises two vertical zones of slightly lower amplitudes that terminate at bright spots about 50 m beneath an ~15 m deep seafloor depression (Figure 5b). The anomaly is also marked by strong up-bending of reflections. Its location corresponds to the “plume field” sample site of Fisher et al. [2011].

**Table 2.** Heat Flow Probe Measurements of the Geothermal Gradient and Thermal Conductivity *k* on Cruise MSM21-4, and the Resulting Heat Flow

station	Latitude (°N)	Longitude (°E)	no. of T sensors (of 22 total)	grad T (°C km <sup>-1</sup> )	no. of <i>k</i> sensors (of 22 total)	<i>k</i> mean (W m <sup>-1</sup> K <sup>-1</sup> )	resulting heat flow (mW m <sup>-2</sup> )
622	78.5100	7.1180	22	142.8	12	1.74	246.9
623	78.5192	7.2705	22	73.5	10	1.71	124.9
624	78.5250	7.3650	22	72.7	21	1.45	107.9
625	78.5545	7.8425	22	88.7	21	1.33	110.6

#### 4.4. Heat Flow

##### 4.4.1. BSR-Derived Heat Flow

The BSR-derived heat flow ranges between  $\sim 80 \text{ mW m}^{-2}$  and  $330 \text{ mW m}^{-2}$ , with 90% of the values being in the order of  $100\text{--}140 \text{ mW m}^{-2}$  (Figure 6a). The geothermal gradient varies between  $\sim 60^\circ\text{C km}^{-1}$  and  $260^\circ\text{C km}^{-1}$  (90% between  $80^\circ\text{C km}^{-1}$  and  $130^\circ\text{C km}^{-1}$ ). In general, heat flow increases from the continental slope toward the Knipovich Ridge and the Molloy TF (Figure 6a). This trend is also supported by the average heat flow values, which are higher for the MSM21/4 data ( $120 \text{ mW m}^{-2}$ ) than for the JR211 data ( $109 \text{ mW m}^{-2}$ ), which were collected closer to the continental slope. About 0.5% of the BSR-derived heat flow values exceed  $300 \text{ mW m}^{-2}$ . These high values occur at the center of the rift zone, at the transition of the Knipovich Ridge and the Molloy TF (Figure 6a).

##### 4.4.2. Heat Flow Probe Measurements

The geothermal gradient derived from the temperature measurements of the four heat flow probe ranges between  $72.7^\circ\text{C km}^{-1}$  and  $142.8^\circ\text{C km}^{-1}$  (Table 2). Together with the mean thermal conductivity, these values resulted in heat flow between  $\sim 110 \text{ mW m}^{-2}$  and  $\sim 250 \text{ mW m}^{-2}$  (Table 2). However, the thermal conductivities (Table 2) are associated with a high uncertainty, especially at the two western stations (622 and 623; Figure 6b) where the probe did not fully penetrate into the sediment and only about half of the thermal conductivity sensors recorded values. Consequently, thermal conductivity values and hence heat flow values may be too high at these stations.

Additional but smaller errors are associated with the measurement itself, which had a precision of  $0.002^\circ\text{C}$ , and the estimation of the geothermal gradient. Although the recorded temperatures did not scatter greatly, allowing a reliable estimation of the geothermal gradient through linear regression (Figure S2 in the supporting information), the geothermal gradient may have been influenced by seasonal temperature variations in the shallow sedimentary sections, as observed on the Svalbard margin [Berndt *et al.*, 2014b].

A direct comparison of measured and BSR-derived heat flow values was not possible as a BSR was not observed at any of the heat flow stations. Still, the  $\sim 108 \text{ mW m}^{-2}$  and  $\sim 110 \text{ mW m}^{-2}$  at the two eastern stations (624 and 625; Figure 6b) agree well with the calculated heat flow of nearby BSR sections (Figure 6a).

#### 4.5. Modeling Results

In general, the modeling results show that bulk petroleum production (i.e., oil and gas) occurs at all three sites (site A, site B, and Site 909) for each source rock scenario. However, the generated mass of hydrocarbons at Site 909 is two magnitudes lower than at sites A and B.

For the true stratigraphy of Site 909, which included the Miocene source rock, production did not occur until middle Miocene (10 Ma). Until present, it reached a generated mass of  $\sim 0.3 \text{ kt}$ , assuming mean TOC and HI values (Run 1; Figure 7a). When the Eocene source rock was added underneath, production started earlier ( $\sim 40 \text{ Ma}$ ) but remained almost zero until  $\sim 14 \text{ Ma}$ , when it began to increase to  $\sim 1.2 \text{ kt}$  (again for mean TOC and HI) until present (Figure 7a).

For Run 2 (Miocene and Eocene source rock), no significant production occurred at site A until middle Miocene (Figure 7c). A strong increase in production took place between 15 Ma and 10 Ma, reaching a generated mass of  $0.07 \text{ Mt}$  (for mean TOC and HI;  $0.19 \text{ Mt}$  for maximum) until present. The associated burial curve (Figure 7b) shows a rapid increase of overburden ( $\sim 2000 \text{ m}$ ) in the interval of 15–10 Ma, corresponding to the timing of the production increase.

Unlike site A, site B was characterized by two production phases in Run 2: the first phase occurred in the Eocene prior to  $\sim 40 \text{ Ma}$ , while the second phase began in middle Miocene at  $\sim 14 \text{ Ma}$  (Figure 7d). The second phase was marked by a strong increase in production until 10 Ma, followed by reduced production until present ( $\sim 0.07 \text{ Mt}$  for mean TOC and HI,  $\sim 0.19 \text{ Mt}$  for maximum).

In contrast to Run 2, the results of Run 3 (Miocene source rock only) were relatively similar for sites A and B (Figures 7e and 7f). At both sites, hydrocarbon production started at 13.5 Ma and increased rapidly until 10 Ma, although the increase was stronger at site A than at site B. At site A, the bulk production until present was  $\sim 0.11 \text{ Mt}$  for mean TOC and HI ( $\sim 0.19 \text{ Mt}$  for maximum); at site B, it was slightly lower ( $\sim 0.10 \text{ Mt}$  for mean,  $\sim 0.18 \text{ Mt}$  for maximum TOC and HI).

When layer thicknesses were gradually increased from the thicknesses determined at Site 909 to those used for Run 3, the generated mass of hydrocarbons also increased (Run 4; Figures 7g and 7h). At site A, the bulk

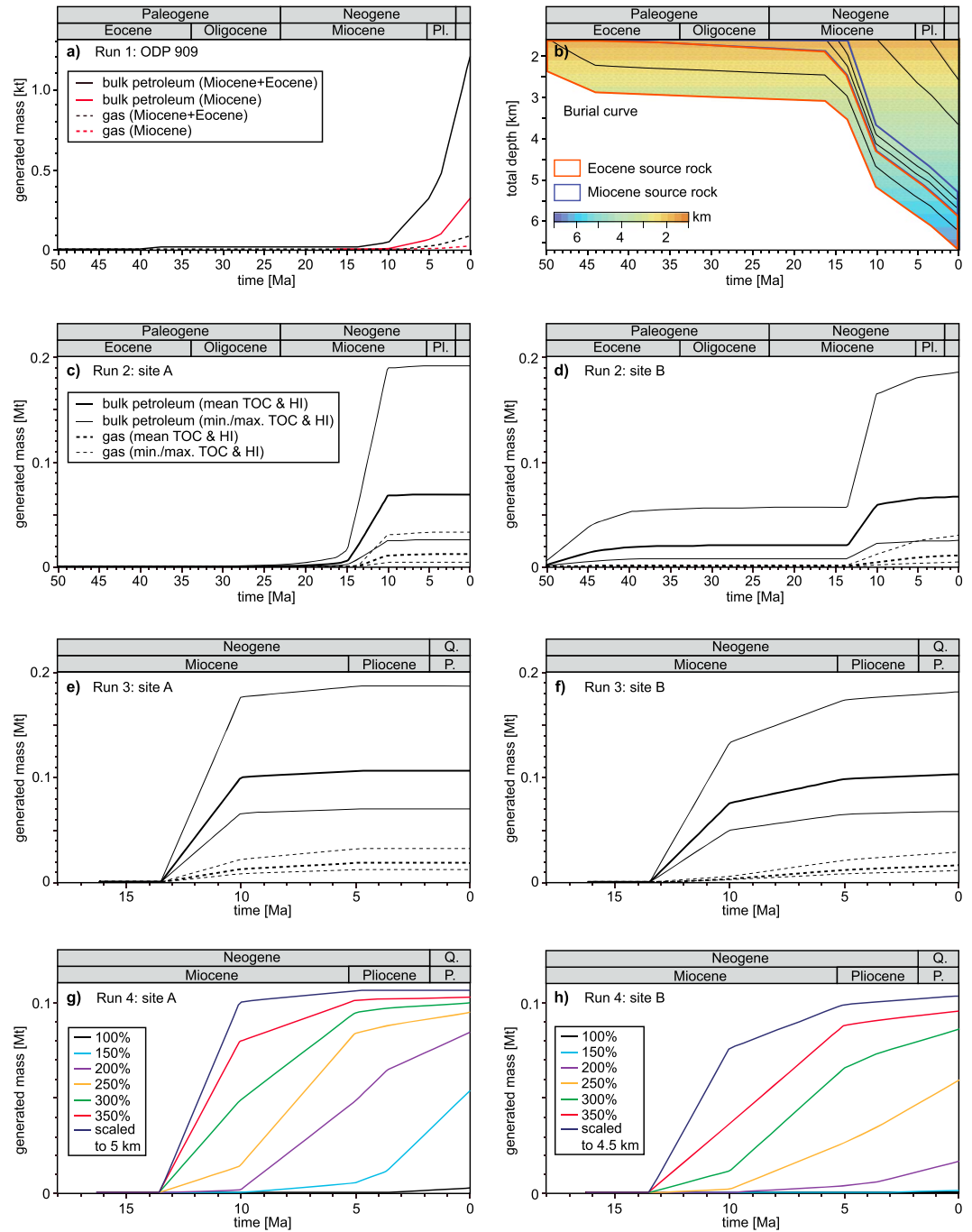


**Figure 7.** Results of the 1-D petroleum system modeling. Curves for min. and max. TOC and HI represent error bounds of the model. (a) Run 1 for Miocene (red) and Miocene and Eocene (black) source rocks at ODP Site 909. (b) Burial curve for site A (Run 2A). (c) Hydrocarbon generation for Miocene and Eocene source rocks at site A (Run 2A). (d) Hydrocarbon generation for Miocene and Eocene source rocks at site B (Run 2B). Note that there are two generation phases, one in the Eocene and one in the middle Miocene. (e) Hydrocarbon generation for a Miocene source rock at site A (Run 3A). (f) Hydrocarbon generation for a Miocene source rock at site B (Run 3B). (g) Hydrocarbon generation for varying total sediment thicknesses in percentages of sediment thicknesses at Site 909 (site A). (h) Hydrocarbon generation for varying total sediment thicknesses in percentages of sediment thicknesses at Site 909 (site B). Note that the generated mass is given in kt in Figure 7a and in Mt for Figures 7c–7h. Legend for Figures 7d–7f is shown in Figure 7c.

petroleum production for mean TOC and HI increased from  $<0.01$  Mt for 100% layer thicknesses of Site 909 to  $>0.10$  Mt for the layer thicknesses of Run 3 (Figure 7g). At site B, production also increased to  $>0.10$  Ma for the thicknesses of Run 3; however, hydrocarbon generation did not occur for 100% layer thicknesses of Site 909 (Figure 7h).

With increasing overburden, hydrocarbon production started earlier. At site A, the onset of production changed from  $\sim 3.5$  Ma for the 100% case to  $\sim 13.5$  Ma for the layer thicknesses of Run 3 (Figure 7g). Similarly, at site B the onset changed from  $\sim 3.0$  Ma (150%) to  $\sim 13.5$  Ma for Run 3 thicknesses (Figure 7h).

The slope of the production curves, and hence the production rate, also changed with increasing overburden. For a thicker overburden ( $>300\%$ ), production started with relatively high rates and slowed down around 11–10 Ma and at the beginning of the Pliocene (Figures 7g and 7h). For a thinner overburden ( $<300\%$ ), production rates were initially low but increased at  $\sim 10$  Ma. In the Pliocene, production rates then either decreased (e.g., for 200% and 250% at site A) or increased (e.g., 150% at site A).

At site A, the production curves leveled off in the Pliocene for the 350% and Run 3 curves, i.e., production ceased in Pliocene times (Figure 7g). Saturation was neither observed in the other curves nor at site B. Instead, production is presently ongoing at different rates. The highest present-day rates occur for the 150% case at site A and 250% at site B.

## 5. Discussion

### 5.1. Fluid Migration

Compared to Vestnesa Ridge [e.g., Büinz *et al.*, 2008, 2012], there are not many indications for vertical fluid migration in the seismic data of our study area. In the study area, potential pathways for vertical fluid migration are faults and pipe structures [Hustoft *et al.*, 2009; Sarkar *et al.*, 2012].

We interpret the undisturbed BSR at the faults to indicate that the faults are probably not actively transporting fluids. This is in agreement with the absence of seismic amplitude anomalies in seismic data adjacent to the faults, and with Sarkar *et al.* [2012], who could not find evidence for fault-controlled gas migration in the shallow parts of the Svalbard margin. We note, however, that fluid dissipation could take place along the faults but not fast enough to affect the thermal field and the BSR.

In contrast, the interruption of the BSR at the pipe structures indicates a disruption of the thermal field. The chaotic reflection character within the down-bending pipes, as well as bright spots at other pipes, suggests the presence of free gas and therefore the possibility of vertical fluid migration. At the two pipes that reach the seafloor, active fluid venting could possibly be going on, but sediment cores taken in the vicinity did not show signs of active seepage. The pipe structures that do not reach the seafloor may either be still-developing structures or extinct and buried.

Although it seems more likely that fluid migration occurs at pipe structures than at faults, the small number of potential fluid flow features suggests that vertical fluid migration is presently very limited in the study area. Vanneste *et al.* [2005b] propose that the outer Svalbard margin is undergoing extension and that the long and continuous BSR and its bottom-simulating behavior indicate that this extension has not yet affected the fluid flow system. However, the role of fluid migration could increase in the future, which would cause a more irregular and less seabed-following BSR [Vanneste *et al.*, 2005b]. Both the absence of fluid migration markers and the undisturbed BSR indicate that the strata above the BSR are not strongly affected by gas production at depth and that gas ascending to the BGHSZ turns into hydrate instead of penetrating the GHSZ.

### 5.2. Source Rock Potential in the Study Area

Due to the lack of information on some of the modeling input parameters, several assumptions had to be made that affected the final outcome of the petroleum system modeling. While the geological model is relatively well constrained, uncertainties are high for the heat flow evolution at the modeling sites and for the kinetics of hydrocarbon generation. We therefore refrain from discussing the exact amounts of hydrocarbons that are potentially generated, but only consider the general trends.

Given the assumptions discussed in section 3.4.2, hydrocarbons, including oil and gas, form from the Miocene source rock north of the Knipovich Ridge. Even if sediment thicknesses at the modeling sites

are not as assumed for Run 3 (Figures 7e and 7f), the results of Run 4 (Figures 7g and 7h) show that lower total sediment thicknesses still allow hydrocarbon production at both site A and site B. Production also occurs at Site 909 (Run 1; Figure 7a), although the generated mass is small in comparison. However, if production occurs at Site 909 where the Cenozoic sediments are thinnest, then it is reasonable to assume that production is also possible further landward where sediment thicknesses are greater [Ritzmann *et al.*, 2004].

Our results support the idea of Smith *et al.* [2014], who suggested that thermogenic gas on Vestnesa Ridge could be related to hydrocarbon production from Miocene source rocks. Extensive hydrocarbon production during the Miocene thus probably led to increased hydrate formation, which is reflected by the widespread BSR in the Knipovich area. However, due to the large input-associated uncertainties of the generated mass of hydrocarbons, we cannot tell if the generated amount is sufficient to explain the wide lateral distribution of gas inferred from the BSR extent.

In the case that both a Miocene and an Eocene source rock are present in the study area, it is not possible to derive from the production curves whether both source rocks contributed to the generated amount of hydrocarbons observed. However, the results of site A (Figure 7c) show that if hydrocarbons are produced from Eocene sediments, the Eocene source rock is not mature enough until Miocene times. This is different for site B (Figure 7d), where an Eocene as well as a Miocene production phase are observed—with the Eocene phase obviously being related to the Eocene source rock. Thus, during the Eocene the source rock was sufficiently mature for hydrocarbon production at site B but not at site A, even though the two sites are only ~30 km apart.

Similar observations were made in the Arctic Basin where the same Eocene source rock is mature in the Amundsen Basin but not at the adjacent Lomonosov Ridge [Mann *et al.*, 2009]. Mann *et al.* [2009] attributed the difference to the higher overburden and deeper burial in the Amundsen Basin. In our study area, however, a higher overburden cannot explain the observed differences during the Eocene as there was no overburden above the Eocene source rock. We therefore need to consider other parameters.

Apart from the sedimentary overburden, parameters that influence modeled source rock maturity and hydrocarbon generation are organic matter characteristics, kinetics of hydrocarbon generation, and heat flow. Organic matter characteristics were assumed to be the same at sites A and B, as were the kinetics of hydrocarbon generation. Heat flow, however, differed: during the Eocene, heat flow was high (200–300 mW m<sup>-2</sup>) at site B and low (60–70 mW m<sup>-2</sup>) at site A, due to the close proximity of site B to the Eocene spreading center. We believe that the Eocene heat flow was high enough to cause hydrocarbon generation at site B but not at site A.

The difference in heat flow also explains why there were two phases of hydrocarbon generation at site B and only one at site A. The Eocene phase was mainly controlled by temperature, i.e., heat flow, which was too low at site A to induce production. In the Miocene phase, heat flow was similar at both sites (Figure 2b). This phase appears instead to be controlled by sediment deposition as indicated by the burial curve (Figure 7b), which shows rapid burial during 15–10 Ma, coeval with the second phase of hydrocarbon generation.

As the heat flow in the study area is strongly controlled by the Knipovich Ridge, which is inferred from heat flow increasing toward the ridge axis (Figure 6a), the Eocene phase of hydrocarbon generation appears to be influenced by the Knipovich Ridge. In contrast, the Miocene phase seems largely independent from the ridge and is controlled primarily by sedimentation processes.

### 5.3. Conditions for the Existence of Eocene Rocks at the Northern End of the Knipovich Ridge

It is not known if the same source rock as in the Arctic Basin also exists in our study area. The only stratigraphic information for the Svalbard margin comes from ODP sites, which have not been drilled down to the depths of potential Eocene sequences [Myhre *et al.*, 1995]. It is therefore important to consider the conditions under which an Eocene source rock similar to that of the Arctic Basin could have been deposited on the Svalbard margin.

The Eocene source rock found in the Arctic Basin is associated with the deposition of the fern *Azolla* during early to middle Eocene [Brinkhuis *et al.*, 2006; Mann *et al.*, 2009]. Conditions for the deposition of *Azolla*, which

is a freshwater plant, include well-stratified waters and “Black-Sea-type” anoxia [Brinkhuis *et al.*, 2006] that are generally restricted to relatively closed basins. The Arctic Ocean remained a closed basin until the Miocene [Jakobsson *et al.*, 2007], thus allowing no exchange of organic matter. However, the deposition of *Azolla* was not limited to the Arctic Basin. Brinkhuis *et al.* [2006] show that *Azolla* deposits were found as far south as the North Sea, including in Svalbard, although they do not give an exact location.

If *Azolla*-derived organic matter was deposited on the Svalbard margin, it must have occurred in a closed basin setting. Multiple basins may have existed during the Eocene, in the form of pull-apart basins that were part of the ancient Spitsbergen Shear Zone [Crane *et al.*, 1982, 2001]. These pull-apart basins later developed into mid-ocean ridge segments offset by transform faults, such as the Molloy Ridge and Transform Fault [Crane *et al.*, 1982; Thiede *et al.*, 1990]. It is therefore possible that there was also a pull-apart basin, e.g., similar to today's Molloy Deep, north of the Knipovich Ridge.

In such pull-apart basins, favorable conditions for the deposition of *Azolla* could have been met and maintained into the early stage of rifting, thus enabling the development of a source rock comparable to that found in the Arctic Basin. Brinkhuis *et al.* [2006] note that during the middle Eocene, surface waters of the Atlantic Ocean were sufficiently fresh for *Azolla* to grow and spread. Nevertheless, it remains speculative that *Azolla*-derived organic matter was deposited in our study area during the Eocene and resulted in the formation of a sufficiently thick source rock sequence. Without deeper drilling, the existence of an Eocene source rock on the western Svalbard margin cannot be proved.

#### 5.4. Discussion of the Results in the Light of Thermogenic Gas Finds on Vestnesa Ridge

Our results are consistent with the observation of thermogenic gas at Vestnesa Ridge. First, we observe a widespread BSR in an area of increased heat flow, i.e., at the intersection of the Knipovich Ridge and the Molloy TF. Second, the petroleum system modeling shows that in situ thermogenic hydrocarbon production, including gas, is possible from both existing Miocene sediments and a potential Eocene source rock. Consequently, some hydrocarbon generation must have occurred on the Svalbard margin, which is in agreement with the thermogenic gas finds of Fisher *et al.* [2011] and Smith *et al.* [2014].

Alternatively, serpentinization could be a source for extensive gas hydrate occurrence. Serpentinization requires seawater to enter the upper mantle, which typically occurs at slow spreading ridges [Minshull *et al.*, 1998]. Serpentinization processes and associated methane generation have been proposed for the central [Kandilarov *et al.*, 2008; Rajan *et al.*, 2012] and southern Knipovich Ridge [Connelly *et al.*, 2007]. In addition, Johnson *et al.* [2015] suggest abiogenic methane generation in the area south of the Molloy TF and west of the Knipovich Ridge. However, methane samples with isotopic signatures that could confirm an abiogenic origin do not exist for any of these areas.

For Vestnesa Ridge, Smith *et al.* [2014] exclude the possibility of serpentinization-derived methane based on the geochemical signatures of the recovered gas hydrate samples. If serpentinization played a role in this area,  $\delta^{13}\text{C}$  values of methane should be heavier than the measured  $-47.7\text{‰}$ , i.e., around  $25\text{‰}$ , but such values were not observed [Smith *et al.*, 2014].

Serpentinization at the northern Knipovich Ridge may have been possible in the early rifting stages when the overburden was thin and the mantle could have been exposed to seawater in places. Since then, however, the oceanic crust has been covered by more than 1 km of sediment, and thus, in order to enable serpentinization, deep-reaching faults would be required that could act as pathways for seawater to the upper mantle. While such faults have been inferred west of the Knipovich Ridge [Johnson *et al.*, 2015], none have been observed in the seismic data from our study area [also Sarkar *et al.*, 2012]. Even if serpentinization did occur in early Eocene, it probably cannot have affected an area large enough to account for the amount of gas observed today.

We cannot completely exclude the possibility of serpentinization-derived methane north of the Knipovich Ridge and the Molloy TF, but we think it unlikely, as this implies that in addition to bacterial production at the slope [Sahling *et al.*, 2014], there are two more methane sources on the Svalbard margin: thermogenic production and serpentinization. Neither the geophysical nor the geochemical data are conclusive about the existence of three separate sources. We therefore share the interpretation of Smith *et al.* [2014] that the gas north of the Knipovich Ridge is mostly of thermogenic origin.

## 6. Conclusions

The western Svalbard margin is characterized by extensive occurrence of gas hydrates with a maximum abundance in the vicinity of the Knipovich Ridge, the Molloy Ridge, and the Lena Trough. The largest area of gas hydrate accumulation inferred from the BSR is north of the Knipovich Ridge. Within this area, heat flow increases from  $80 \text{ mW m}^{-2}$  near the continental slope to  $>300 \text{ mW m}^{-2}$  at the rifting axis.

While bacterial methane is produced at the continental slope and methane associated with serpentinization processes may exist along the central and southern Knipovich Ridge, our results support the interpretation of a thermogenic origin for the gas observed north of the ridge. Petroleum system modeling has shown that the bulk petroleum mass produced since the Eocene is at least 5 kt and could be as high as  $\sim 0.2 \text{ Mt}$ . Thermogenic methane is thus an important contributor to the gas hydrate reservoir on the Svalbard margin.

Although the Knipovich Ridge strongly controls the heat flow distribution on this part of the Svalbard margin, its influence on the amount and timing of thermogenic hydrocarbon production appears minor. The petroleum system modeling shows that thermogenic methane generation happened mainly in the Miocene and is attributed to rapid burial of early Miocene source rocks. However, if Eocene source rocks are present in the study area, hydrocarbon production may also have taken place during the Eocene due to high heat flow in the early stages of rifting. In this case, production would have been strongly influenced by the thermal effects of the Knipovich Ridge.

## Acknowledgments

I.D. was financed by the German Research Foundation (DFG) through the Kiel Cluster of Excellence "The Future Ocean" (EXC80/2-2012). Cruise MSM21/4 was supported by "The Future Ocean" and the DFG. Cruise JR211 was financed by the Natural Environment Research Council as part of the International Polar Year 2007–2008 (grant NE/D005728). Particular thanks are directed to the captains and crew for their excellent support at sea. We also thank Wilfried Jokat (AWI Bremerhaven) for providing additional seismic data. We further thank the Associate Editor and two anonymous reviewers for their constructive comments, which helped to improve the manuscript. The seismic data of cruise MSM21/4 are available at <http://doi.pangaea.de/10.1594/PANGAEA.847497>.

## References

- Berndt, C., et al. (2014a), Fluid dynamics and slope stability offshore W-Spitsbergen: Effect of bottom water warming on gas hydrates and slope stability, Cruise No. MSM21/4, August 12–September 11, 2012, Reykjavik (Iceland) – Emden (Germany), MARIA S. MERIAN-Berichte, MSM21/4, DFG-Senatskommission für Ozeanographie, 96 pp., doi:10.2312/cr\_msm21\_4.
- Berndt, C., et al. (2014b), Temporal constraints on hydrate-controlled methane seepage off Svalbard, *Science*, *343*(6168), 284–287, doi:10.1126/science.1246298.
- Bouriaik, S., M. Vanneste, and A. Saoutkine (2000), Inferred gas hydrates and clay diapirs near the Storegga Slide on the southern edge of the Vøring Plateau, offshore Norway, *Mar. Geol.*, *163*(1–4), 125–148, doi:10.1016/S0025-3227(99)00115-2.
- Brinkhuis, H., et al. (2006), Episodic fresh surface waters in the Eocene Arctic Ocean, *Nature*, *441*(7093), 606–609, doi:10.1038/nature04692.
- Brooks, J. M., H. B. Cox, W. R. Bryant, M. C. Kennicutt II, R. G. Mann, and T. J. McDonald (1986), Association of gas hydrates and oil seepage in the Gulf of Mexico, *Org. Geochem.*, *10*(1–3), 221–234, doi:10.1016/0146-6380(86)90025-2.
- Bünz, S., and J. Mienert (2004), Acoustic imaging of gas hydrate and free gas at the Storegga Slide, *J. Geophys. Res.*, *109*, B04102, doi:10.1029/2003JB002863.
- Bünz, S., J. Mienert, and C. Berndt (2003), Geological controls on the Storegga gas-hydrate system of the mid-Norwegian continental margin, *Earth Planet. Sci. Lett.*, *209*(3–4), 291–307, doi:10.1016/S0012-821X(03)00097-9.
- Bünz, S., J. Mienert, M. Vanneste, and K. Andreassen (2005), Gas hydrates at the Storegga Slide: Constraints from an analysis of multicomponent, wide-angle seismic data, *Geophysics*, *70*(5), B19–B34, doi:10.1190/1.2073887.
- Bünz, S., J. Petersen, S. Hustoft, and J. Mienert (2008), Environmentally-sensitive gas hydrates on the W-Svalbard margin at the gateway to the Arctic Ocean, paper presented at Proceedings of the 6th International Conference on Gas Hydrates, Vancouver, British Columbia, Canada.
- Bünz, S., S. Polyakov, S. Vadakkepuliambatta, C. Consolaro, and J. Mienert (2012), Active gas venting through hydrate-bearing sediments on the Vestnesa Ridge, offshore W-Svalbard, *Mar. Geol.*, *332–334*, 189–197, doi:10.1016/j.margeo.2012.09.012.
- Carcione, J. M., D. Gei, G. Rossi, and G. Madrussani (2005), Estimation of gas-hydrate concentration and free-gas saturation at the Norwegian-Svalbard continental margin, *Geophys. Prospect.*, *53*(6), 803–810, doi:10.1111/j.1365-2478.2005.00502.x.
- Connelly, D. P., C. R. German, M. Asada, K. Okino, A. Egorov, T. Naganuma, N. Pimenov, G. Cherkashev, and K. Tamaki (2007), Hydrothermal activity on the ultra-slow spreading southern Knipovich Ridge, *Geochem. Geophys. Geosyst.*, *8*, Q08013, doi:10.1029/2007GC001652.
- Crane, K., O. Eldholm, A. M. Myhre, and E. Sundvor (1982), Thermal implications for the evolution of the Spitsbergen transform fault, *Tectonophysics*, *89*(1–3), 1–32, doi:10.1016/0040-1951(82)90032-4.
- Crane, K., E. Sundvor, J. P. Foucher, M. Hobart, A. M. Myhre, and S. LeDouaran (1988), Thermal evolution of the western Svalbard margin, *Mar. Geophys. Res.*, *9*(2), 165–194, doi:10.1007/bf00369247.
- Crane, K., E. Sundvor, R. Buck, and F. Martinez (1991), Rifting in the northern Norwegian-Greenland Sea: Thermal tests of asymmetric spreading, *J. Geophys. Res.*, *96*(B9), 14,529–14,550, doi:10.1029/91JB01231.
- Crane, K., H. Doss, P. Vogt, E. Sundvor, G. Cherkashov, I. Poroshina, and D. Joseph (2001), The role of the Spitsbergen shear zone in determining morphology, segmentation and evolution of the Knipovich Ridge, *Mar. Geophys. Res.*, *22*(3), 153–205, doi:10.1023/a:1012288309435.
- Dick, H. J. B., J. Lin, and H. Schouten (2003), An ultra-slow spreading class of ocean ridge, *Nature*, *426*(6965), 405–412, doi:10.1038/nature02128.
- Dickens, G. R., and M. S. Quinby-Hunt (1994), Methane hydrate stability in seawater, *Geophys. Res. Lett.*, *21*(19), 2115–2118, doi:10.1029/94GL01858.
- Ebinger, C. J. (1989), Tectonic development of the western branch of the East African rift system, *Geol. Soc. Am. Bull.*, *101*(7), 885–903, doi:10.1130/0016-7606(1989)101<0885:tdotwb>2.3.co;2.
- Ehlers, B.-M., and W. Jokat (2013), Paleo-bathymetry of the northern North Atlantic and consequences for the opening of the Fram Strait, *Mar. Geophys. Res.*, *34*(1), 25–43, doi:10.1007/s11001-013-9165-9.
- Eiken, O., and K. Hinz (1993), Contourites in the Fram Strait, *Sediment. Geol.*, *82*(1–4), 15–32, doi:10.1016/0037-0738(93)90110-Q.
- Eldholm, O., E. Sundvor, A. M. Myhre, and J. I. Faleide (1984), Cenozoic evolution of the continental margin off Norway and western Svalbard, in *Petroleum Geology of the North European Margin*, edited by A. M. Spencer, pp. 3–18, Springer, Netherlands, doi:10.1007/978-94-009-5626-1\_2.

- Engen, Ø., J. I. Faleide, and T. K. Dyreng (2008), Opening of the Fram Strait gateway: A review of plate tectonic constraints, *Tectonophysics*, 450(1–4), 51–69, doi:10.1016/j.tecto.2008.01.002.
- Expedition 302 Scientists (2006), Sites M0001–M0004, in *Proceedings Integrated Ocean Drilling Program*, vol. 302, edited by J. Backman et al., Integrated Ocean Drilling Program Management International, Inc., Edinburgh.
- Faleide, J. I., A. Solheim, A. Fiedler, B. O. Hjelstuen, E. S. Andersen, and K. Vanneste (1996), Late Cenozoic evolution of the western Barents Sea-Svalbard continental margin, *Global Planet. Change*, 12(1–4), 53–74, doi:10.1016/0921-8181(95)00012-7.
- Fisher, R. E., et al. (2011), Arctic methane sources: Isotopic evidence for atmospheric inputs, *Geophys. Res. Lett.*, 38, L21803, doi:10.1029/2011GL049319.
- Ganguly, N., G. D. Spence, N. R. Chapman, and R. D. Hyndman (2000), Heat flow variations from bottom simulating reflectors on the Cascadia margin, *Mar. Geol.*, 164(1–2), 53–68, doi:10.1016/S0025-3227(99)00126-7.
- Geissler, W. H., W. Jokat, and H. Brekke (2011), The Yermak Plateau in the Arctic Ocean in the light of reflection seismic data-implication for its tectonic and sedimentary evolution, *Geophys. J. Int.*, 187(3), 1334–1362, doi:10.1111/j.1365-246X.2011.05197.x.
- Geissler, W. H., A. C. Gebhardt, and M. C. Schmidt-Aursch (2014a), The Hinlopen/Yermak Megaslide (HYM): Understanding an exceptional submarine landslide, its consequences and relation to the deep structure of the Sophia Basin (Sophia-HYM), Cruise No. MSM31, August 17–September 18, 2013, Tromsø (Norway) - Bremen (Germany), MARIA S. MERIAN-Berichte, MSM31, DFG-Senatskommission für Ozeanographie, 70 pp., doi:10.2312/cr\_msm31.
- Geissler, W. H., P. V. Pulm, W. Jokat, and A. C. Gebhardt (2014b), Indications for the occurrence of gas hydrates in the Fram Strait from heat flow and multichannel seismic reflection data, *J. Geol. Res.*, 12, doi:10.1155/2014/582424.
- Ginsburg, G. D., et al. (1992), Gas hydrates of the Southern Caspian, *Int. Geol. Rev.*, 34(8), 765–782, doi:10.1080/00206819209465635.
- Haacke, R. R., G. K. Westbrook, and R. D. Hyndman (2007), Gas hydrate, fluid flow and free gas: Formation of the bottom-simulating reflector, *Earth Planet. Sci. Lett.*, 261(3–4), 407–420, doi:10.1016/j.epsl.2007.07.008.
- Harvey, L. D. D., and Z. Huang (1995), Evaluation of the potential impact of methane clathrate destabilization on future global warming, *J. Geophys. Res.*, 100(D2), 2905–2926, doi:10.1029/94JD02829.
- Hornbach, M. J., N. L. Bangs, and C. Berndt (2012), Detecting hydrate and fluid flow from bottom simulating reflector depth anomalies, *Geology*, 40(3), 227–230, doi:10.1130/g32635.1.
- Hustoft, S., S. Bünz, J. Mienert, and S. Chand (2009), Gas hydrate reservoir and active methane-venting province in sediments on <20 Ma young oceanic crust in the Fram Strait, offshore NW-Svalbard, *Earth Planet. Sci. Lett.*, 284(1–2), 12–24, doi:10.1016/j.epsl.2009.03.038.
- Ivanov, M., V. Blinova, E. Kozlova, G. K. Westbrook, A. Mazzini, T. Minshull, and H. Nouzé (2007), First sampling of gas hydrate from the Vøring Plateau, *Eos Trans. AGU*, 88(19), 209–212, doi:10.1029/2007EO190001.
- Jakobsson, M., et al. (2007), The early Miocene onset of a ventilated circulation regime in the Arctic Ocean, *Nature*, 447(7147), 986–990, doi:10.1038/nature05924.
- Jakobsson, M., et al. (2012), The International Bathymetric Chart of the Arctic Ocean (IBCAO) version 3.0, *Geophys. Res. Lett.*, 39, L12609, doi:10.1029/2012GL052219.
- Johnson, J. E., J. Mienert, A. Plaza-Faverola, S. Vadakkepuliyambatta, J. Knies, S. Bünz, K. Andreassen, and B. Ferré (2015), Abiotic methane from ultraslow-spreading ridges can charge Arctic gas hydrates, *Geology*, doi:10.1130/G36440.1.
- Kandilarov, A., R. Mjelde, K. Okino, and Y. Murai (2008), Crustal structure of the ultra-slow spreading Knipovich Ridge, North Atlantic, along a presumed amagmatic portion of oceanic crustal formation, *Mar. Geophys. Res.*, 29, 109–134, doi:10.1007/s11001-008-9050-0.
- Kinoshita, M., G. F. Moore, and Y. N. Kido (2011), Heat flow estimated from BSR and IODP borehole data: Implication of recent uplift and erosion of the imbricate thrust zone in the Nankai Trough off Kumano, *Geochem. Geophys. Geosyst.*, 12, Q0AD18, doi:10.1029/2011GC003609.
- Knies, J., and U. Mann (2002), Depositional environment and source rock potential of Miocene strata from the central Fram Strait: Introduction of a new computing tool for simulating organic facies variations, *Mar. Pet. Geol.*, 19(7), 811–828, doi:10.1016/S0264-8172(02)00090-9.
- Knies, J., E. Damm, J. Gutt, U. Mann, and L. Pinturier (2004), Near-surface hydrocarbon anomalies in shelf sediments off Spitsbergen: Evidences for past seepages, *Geochem. Geophys. Geosyst.*, 5, Q06003, doi:10.1029/2003GC000687.
- Kretschmer, K., A. Biastoch, L. Ruepke, and E. Burwicz (2015), Modeling the fate of methane hydrates under global warming, *Global Biochem. Cycles*, 29(5), 610–625, doi:10.1002/2014GB005011.
- Kvarven, T., B. O. Hjelstuen, and R. Mjelde (2014), Tectonic and sedimentary processes along the ultraslow Knipovich spreading ridge, *Mar. Geophys. Res.*, 35(2), 89–103, doi:10.1007/s11001-014-9212-1.
- Kvenvolden, K. A. (1995), A review of the geochemistry of methane in natural gas hydrate, *Org. Geochem.*, 23(11–12), 997–1008.
- Kvenvolden, K. A., M. Golan-Bac, T. J. McDonald, R. C. Pflaum, and J. M. Brooks (1989), Hydrocarbon gases in sediment of the Vøring Plateau, Norwegian Sea, in *Proceedings Ocean Drilling Program, Sci. Results*, vol. 104, edited by O. Eldholm et al., pp. 319–326, Ocean Drilling Program, College Station, Tex.
- Li, L., X. Lei, X. Zhang, and G. Zhang (2012), Heat flow derived from BSR and its implications for gas hydrate stability zone in Shenhu Area of northern South China Sea, *Mar. Geophys. Res.*, 33(1), 77–87, doi:10.1007/s11001-012-9147-3.
- Mann, U., J. Knies, S. Chand, W. Jokat, R. Stein, and J. Zweigel (2009), Evaluation and modelling of Tertiary source rocks in the central Arctic Ocean, *Mar. Pet. Geol.*, 26(8), 1624–1639, doi:10.1016/j.marpetgeo.2009.01.008.
- Martin, V., P. Henry, H. Nouzé, M. Noble, J. Ashi, and G. Pascal (2004), Erosion and sedimentation as processes controlling the BSR-derived heat flow on the Eastern Nankai margin, *Earth Planet. Sci. Lett.*, 222(1), 131–144, doi:10.1016/j.epsl.2004.02.020.
- Mienert, J., J. Posewang, and M. Baumann (1998), Gas hydrates along the northeastern Atlantic margin: Possible hydrate-bound margin instabilities and possible release of methane, *Geol. Soc. Spec. Publ.*, 137(1), 275–291, doi:10.1144/gsl.sp.1998.137.01.22.
- Minshull, T. A., M. R. Muller, C. J. Robinson, R. S. White, and M. J. Bickle (1998), Is the oceanic Moho a serpentinization front?, *Geol. Soc. London, Spec. Publ.*, 148(1), 71–80, doi:10.1144/gsl.sp.1998.148.01.05.
- Myhre, A. M., and O. Eldholm (1988), The western Svalbard margin (74°–80°N), *Mar. Pet. Geol.*, 5(2), 134–156, doi:10.1016/0264-8172(88)90019-0.
- Myhre, A. M., et al. (1995), *Proceedings on ODP, Init. Rep.*, vol. 151, Ocean Drilling Program, College Station, Tex.
- Pepper, A. S., and P. J. Corvi (1995), Simple kinetic models of petroleum formation. Part I: Oil and gas generation from kerogen, *Mar. Pet. Geol.*, 12(3), 291–319, doi:10.1016/0264-8172(95)98381-E.
- Plaza-Faverola, A., S. Bünz, J. E. Johnson, S. Chand, J. Knies, J. Mienert, and P. Franek (2015), Role of tectonic stress in seepage evolution along the gas hydrate-charged Vestnesa Ridge, Fram Strait, *Geophys. Res. Lett.*, 42, 733–742, doi:10.1002/2014GL062474.
- Posewang, J., and J. Mienert (1999), High-resolution seismic studies of gas hydrates west of Svalbard, *Geo-Mar. Lett.*, 19(1), 150–156, doi:10.1007/s003670050102.

- Praeg, D., V. Unnithan, P. M. Shannon, and N. O'Neill (2005), Gas hydrate stability and seabed features in deep-water environments west of Ireland, and. Geosphere-Biosphere Coupling Processes: The TTR Interdisciplinary Approach Towards Studies of the European and North African Margins, Marrakech, Morocco, 2–5 February, 2005; *UNESCO, IOC Workshop Rep. 197*, pp. 24–25.
- Rajan, A., J. Mienert, S. Bünz, and S. Chand (2012), Potential serpentinization, degassing, and gas hydrate formation at a young (<20 Ma) sedimented ocean crust of the Arctic Ocean ridge system, *J. Geophys. Res.*, *117*, B03102, doi:10.1029/2011JB008537.
- Ritzmann, O., W. Jokat, W. Czuba, A. Guterch, R. Mjelde, and Y. Nishimura (2004), A deep seismic transect from Hovgård Ridge to northwestern Svalbard across the continental-ocean transition: A sheared margin study, *Geophys. J. Int.*, *157*(2), 683–702, doi:10.1111/j.1365-246X.2004.02204.x.
- Sahling, H., et al. (2014), Gas emissions at the continental margin west of Svalbard: mapping, sampling, and quantification, *Biogeosciences*, *11*(21), 6029–6046, doi:10.5194/bg-11-6029-2014.
- Sarkar, S., C. Berndt, T. A. Minshull, G. K. Westbrook, D. Klaeschen, D. G. Masson, A. Chabert, and K. E. Thatcher (2012), Seismic evidence for shallow gas-escape features associated with a retreating gas hydrate zone offshore west Svalbard, *J. Geophys. Res.*, *117*, B09102, doi:10.1029/2011JB009126.
- Sarkar, S., K. L. Sheen, D. Klaeschen, J. A. Brearley, T. A. Minshull, C. Berndt, R. W. Hobbs, and A. C. Naveira Garabato (2015), Seismic reflection imaging of mixing processes in Fram Strait, *J. Geophys. Res. Oceans*, *120*, 6884–6896, doi:10.1002/2015JC011009.
- Shipboard Scientific Party (1995a), Site 908, in *Proceedings on ODP, Init. Rep.*, vol. 151, edited by A. M. Myhre et al., pp. 113–158, Ocean Drilling Program, College Station, Tex.
- Shipboard Scientific Party (1995b), Site 909, in *Proceedings on ODP, Init. Rep.*, vol. 151, edited by A. M. Myhre et al., pp. 159–220, Ocean Drilling Program, College Station, Tex.
- Shibley, T. H., M. H. Houston, R. T. Buffler, F. J. Shaub, K. J. McMillen, J. W. Ladd, and J. L. Worzel (1979), Seismic evidence for widespread possible gas hydrate horizons on continental slopes and rises, *AAPG Bull.*, *63*(12), 2204–2213.
- Sloan, E. D. (1998), *Clathrate Hydrates of Natural Gases*, Marcel Dekker, New York.
- Smith, A. J., J. Mienert, S. Bünz, and J. Greinert (2014), Thermogenic methane injection via bubble transport into the upper Arctic Ocean from the hydrate-charged Vestnesa Ridge, Svalbard, *Geochem. Geophys. Geosyst.*, *15*, 1945–1959, doi:10.1002/2013GC005179.
- Spielhagen, R., K. Werner, S. A. Sørensen, K. Zamelczyk, E. Kandiano, G. Budeus, K. Husum, T. M. Marchitto, and M. Hald (2011), Enhanced modern heat transfer to the Arctic by warm Atlantic water, *Science*, *331*(6016), 450–45, doi:10.1126/science.1197397.
- Stein, R. (2007), Upper Cretaceous/lower Tertiary black shales near the North Pole: Organic-carbon origin and source-rock potential, *Mar. Pet. Geol.*, *24*(2), 67–73, doi:10.1016/j.marpetgeo.2006.10.002.
- Stein, R., and R. Stax (1996), Organic carbon and *n*-alkane distribution in Late Cenozoic sediments of Arctic Gateways sites 909 and 911 and their paleoenvironmental implications: Preliminary results, in *Proceedings Ocean Drilling Program, Sci. Results*, vol. 151, edited by J. Thiede et al., pp. 391–405, Ocean Drilling Program, College Station, Tex.
- Stein, R., B. Boucsein, and H. Meyer (2006), Anoxia and high primary production in the Paleogene central Arctic Ocean: First detailed records from Lomonosov Ridge, *Geophys. Res. Lett.*, *33*, L18606, doi:10.1029/2006GL026776.
- Sundvor, E., O. Eldholm, T. P. Gladczenko, and S. Planke (2000), Norwegian-Greenland Sea thermal field, *Geol. Soc. Spec. Publ.*, *167*, 397–410.
- Svensen, H., S. Planke, A. Malthe-Sørensen, B. Jamtveit, R. Myklebust, T. Rasmussen Eidem, and S. S. Rey (2004), Release of methane from a volcanic basin as a mechanism for initial Eocene global warming, *Nature*, *429*(6991), 542–545.
- Talwani, M., and O. Eldholm (1977), Evolution of the Norwegian-Greenland Sea, *Geol. Soc. Am. Bull.*, *88*(7), 969–999, doi:10.1130/0016-7606(1977)88<969:eotns>2.0.co;2.
- Thiede, J., S. Pfirman, H.-W. Schenke, and W. Reil (1990), Bathymetry of Molloy Deep: Fram Strait between Svalbard and Greenland, *Mar. Geophys. Res.*, *12*(3), 197–214, doi:10.1007/bf02266713.
- Townend, J. (1997), Estimates of conductive heat flow through bottom-simulating reflectors on the Hikurangi and southwest Fiordland continental margins, New Zealand, *Mar. Geol.*, *141*(1–4), 209–220, doi:10.1016/S0025-3227(97)00073-X.
- Vanneste, M., S. Guidard, and J. Mienert (2005a), Arctic gas hydrate provinces along the western Svalbard continental margin, *Nor. Pet. Soc. Spec. Publ.*, *12*, 271–284, doi:10.1016/S0928-8937(05)80054-2.
- Vanneste, M., S. Guidard, and J. Mienert (2005b), Bottom-simulating reflections and geothermal gradients across the western Svalbard margin, *Terra Nova*, *17*(6), 510–516, doi:10.1111/j.1365-3121.2005.00643.x.
- Villinger, H., and E. E. Davis (1987), A new reduction algorithm for marine heat flow measurements, *J. Geophys. Res.*, *92*(B12), 12,846–12,856, doi:10.1029/JB092IB12p12846.
- Vogt, P. R., and E. Sundvor (1996), Heat flow highs on the Norwegian-Barents-Svalbard continental slope: Deep crustal fractures, dewatering, or “memory in the mud”? *Geophys. Res. Lett.*, *23*(24), 3571–3574, doi:10.1029/96GL03259.
- Vogt, P. R., K. Crane, E. Sundvor, B. O. Hjelstuen, J. Gardner, F. Bowles, and G. Cherkashev (1999), Ground-truthing 11- to 12-kHz side-scan sonar imagery in the Norwegian-Greenland Sea: Part II: Probable diapirs on the Bear Island fan slide valley margins and the Vøring Plateau, *Geo-Mar. Lett.*, *19*(1–2), 111–130, doi:10.1007/s003670050099.
- Westbrook, G. K., et al. (2008), Estimation of gas hydrate concentration from multi-component seismic data at sites on the continental margins of NW Svalbard and the Storegga region of Norway, *Mar. Pet. Geol.*, *25*(8), 744–758, doi:10.1016/j.marpetgeo.2008.02.003.
- Westbrook, G. K., et al. (2009), Escape of methane gas from the seabed along the West Spitsbergen continental margin, *Geophys. Res. Lett.*, *36*, L15608, doi:10.1029/2009GL039191.
- Yamano, M., S. Uyeda, Y. Aoki, and T. H. Shipley (1982), Estimates of heat flow derived from gas hydrates, *Geology*, *10*(7), 339–343, doi:10.1130/0091-7613(1982)10<339:eohtdf>2.0.co;2.